Heat and Mass Transfer in Pulsed-Laser-Induced Phase Transformations

COSTAS P. GRIGOROPOULOS, TED D. BENNETT,
JENG-RONG HO, XIANFAN XU,* AND XIANG ZHANG

Department of Mechanical Engineering, University of California, Berkeley, California

I. Pulsed Laser Melting

A. BACKGROUND

In terms of heat transfer, the fundamental question raised in this chapter is whether essential features of pulsed laser melting and resolidification at the nanosecond time scale can be described using a thermal model. Of specific interest is the description of the transient melting front propagation as a function of the induced temperature field. Several techniques have been developed to probe the transient temperature field during pulsed laser processing. However, as will become apparent, every technique has inherent limitations suitable only for particular materials, temperature ranges, spatial constraints, and so forth. A standard time-of-flight measurement was used to measure the lattice temperature of bulk crystalline silicon during pulsed ruby laser heating [96]. This method involves measurement of the kinetic energy of particles released from the surface of the material. A characteristic temperature is extracted by fitting equilibrium Maxwellian distributions to the translational kinetic-energy data. However, the derivation of the temperature is based on the assumption that the ejected particles are in a thermal equilibrium state. Such an assumption may not be valid, particularly when the sputtering mechanism

*Present address: School of Mechanical Engineering, Purdue University, West Lafayette, IN 47907.

is nonthermal. Transient temperature during nanosecond Nd:glass laser irradiation was also measured using an iron-constantan thin-film thermo-couple [6]. A similar thermistor technique [55] was applied to study the interface temperature of SiAs alloys during planar-interface solidification induced by a pulsed XeCl excimer laser. The complicated sample prepara-tion involved in these two methods limits their usefulness for direct noncontact temperature monitoring of materials. The optical reflectivity technique [46] is the most widely used method to study the pulsed-laser-induced phase transformation and probe the transient temperature field. To obtain the temperature information by the optical reflectivity method, the temperature dependence of the optical properties (i.e., the complex refractive index) must be known. The sensitivity of this optical technique is reduced as the variation of reflectivity with temperature is decreased. Numerical heat transfer computations are used to obtain the transient temperature field [86, 108–110].

In this section, the pulsed laser melting process induced by nanosecond-length ultraviolet (UV) excimer laser pulses is examined. The main advan-tage in using UV radiation is the short optical penetration depth, which for metals and semiconductors is of the order of tens of nanometers. The excimer beam spatial distribution exhibits inhomogeneities (i.e., hot spots) but can be made uniform using homogenizers. Beam uniformity is essential for quantitative experimentation and for applications such as mask projection machining. The size of a focused excimer laser spot in most applications is of the order of millimeters, i.e. much larger than the absorption penetration depth and the thermal penetration depth in the target solid, $\delta_T \sim \sqrt{\alpha \tau_p}$, which is on the order of micrometers. Thus, the transient melting process is usually understood as a one-dimensional phenomenon. This simplification may not be adequate for modeling micro-machining processes, where the thermal penetration depth becomes com-parable with the micromachined feature size. It should, however, be mentioned that the smallest feature achievable with excimer laser technol-ogy is, in principle, determined by the optical diffraction limit, which scales with the short UV wavelengths (0.19–0.30 μm).

B. THERMAL MODELING

Two methods are commonly used for computational handling of heat transport with phase change: (1) the *enthalpy method*, which is suitable for problems not requiring precise information about the liquid–solid inter-face not requiring and (2) *interface tracking method*, which utilizes a change of coordinates that allows an exact boundary condition to be imposed on

the moving interface at all times. Both methods are founded on the Fourier law for heat transport. Instead of the classical Fourier heat diffusion model, the hyperbolic heat conduction [54, 75, 80] and the vibrational cooling model [22] have been proposed. However, the mean free time between electron collisions in a metallic conductor and the relaxation time of electronic events in semiconductors are in the subpicosecond regime. Thus, for the nanosecond-length laser pulses considered in this work, it may be assumed that the laser light energy is immediately redistributed and passed on to the lattice and converted into heat at the location of absorption. Therefore, it is reasonable to assume a local thermodynamic equilibrium state, and the conventional concept of temperature and thermal properties can be defined and used in this study.

In the enthalpy formulation approach [5, 89], the position of the interface does not appear explicitly in the calculation. The enthalpy function is used to account for phase change. In the regions to either side of the melting temperature zone, where $T < T_m$ and $T > T_m$, where T_m is the melting temperature, the enthalpies are

$$H(T) = \int_0^T \rho(T) C_p(T) \, dT; \qquad T < T_m \tag{1}$$

$$H(T) = \int_0^T \rho(T) C_p(T) \, dT + L_m; \qquad T > T_m. \tag{2}$$

For $T = T_m$ the enthalpy function assumes values between H_{sm} and H_{lm}, where

$$H_{sm} = \int_0^{T_m} \rho(T) c_p(T) \, dT \tag{3}$$

$$H_{lm} = \int_0^{T_m} \rho(T) C_p(T) \, dT + L_m. \tag{4}$$

The enthalpy value $H = H_{sm}$ is assigned to solid material at the melting temperature, whereas $H = H_{lm}$ corresponds to pure liquid phase at the same temperature. Thus, there is a region of partial melting, defined by

$$H_{sm} < H < H_{lm}; \qquad T = T_m. \tag{5}$$

Each point within this region can be assigned a solid fraction $f_s(x, t)$ and a liquid fraction $f_l(x, t)$, for which

$$f_s(x, t) + f_l(x, t) = 1. \tag{6}$$

Thus, the enthalpy function during melting at $T = T_m$ is given by

$$H = H_{sm} + f_l L_m. \tag{7}$$

Using enthalpy as a dependent variable, along with the temperature, the heat conduction in the target material is written

$$\frac{\partial H(T)}{\partial t} = \frac{\partial}{\partial x}\left(k(T)\frac{\partial T}{\partial x}\right) + Q_{ab}(x,t).$$ (8)

The excimer laser absorption penetration depth in the thin film, $d_{ab} = 1/\eta$, is of the order of 10 nm [91], where η is the absorption coefficient. Assuming that the target material thickness is at least a few times larger than d_{ab}, the energy absorption, $Q_{ab}(x,t)$, follows an exponential decay:

$$Q_{ab}(x,t) = (1 - R_{exc})I(t)\eta e^{-\eta x}.$$ (9)

The normal reflectivity of silicon surface is given by

$$R_{exc} = \frac{(n_{exc} - 1)^2 + k_{exc}^2}{(n_{exc} + 1)^2 + k_{exc}^2}.$$ (10)

The absorption coefficient η is calculated as

$$\eta = \frac{4\pi k_{exc}}{\lambda_{exc}}.$$ (11)

Incident laser intensity is typically high enough for convection and radiation losses from the top surface to be negligible. Also, for nanosecond time scales the temperature penetration is small, so that the bulk material is maintained at the ambient temperature, T_∞:

$$\frac{\partial T}{\partial x}\bigg|_{x=0} = 0,$$ (12a)

$$T(x = d_{ss}, t) = T_\infty.$$ (12b)

Initially the target is isothermal, at the ambient temperature:

$$T(x,0) = T_\infty.$$ (13)

These equations can be easily solved by implementing an implicit or explicit finite-difference algorithm on a fixed grid.

In contrast to the enthalpy method, the heat conduction equation can also be cast using temperature as the sole dependent variable:

$$(\rho C_p)(T)\frac{\partial T}{\partial t} = \frac{\partial}{\partial x}\left(k(T)\frac{\partial T}{\partial x}\right) + Q_{ab}(x,t).$$ (14)

A system of coordinates attached to the moving interface can now be considered. The transient position of the moving interface, measured from the location of the exposed surface at $t = 0$, is given by the function

$X_{int}(t)$. The heat conduction equation is written in this system of coordinates:

$$(\rho C_p)(T)\left[\frac{DT}{Dt} - \frac{\partial T}{\partial x}\frac{dx}{dt}\right] = \frac{\partial}{\partial x}\left(k(T)\frac{\partial T}{\partial x}\right) + Q_{ab}(x,t). \quad (15)$$

Interface tracking schemes apply the exact boundary conditions at the moving solid/liquid-phase boundary. The energy transfer is balanced across the moving interface, which is at temperature T_{int}:

$$T_s(X_{int}) = T_l(X_{int}) = T_{int}, \quad (16a)$$

$$k_s\frac{\partial T_s}{\partial x}\bigg|_{x=X_{int}} - k_l\frac{\partial T_l}{\partial x}\bigg|_{x=X_{int}} = \rho_s L_m V_{int}. \quad (16b)$$

If no superheating or undercooling is assumed, the interface is at the equilibrium melting temperature, T_m. Melt–solid-interface velocities in pulsed laser melting and recrystallization can exceed 15 m/s [45, 67]. For such velocities, the liquid phase is expected to be highly overheated or undercooled and the assumption of a constant, thermodynamic equilibrium, phase-change temperature is no longer valid [43]. According to the quasi-chemical formulation of crystal growth from the melt [43, 44] the rate at which atoms join the crystal is

$$R_F = R_F^\circ \exp\left[-\frac{Q}{k_B T_{int}}\right], \quad (17)$$

where k_B is Boltzmann's constant, T_{int} is the interface temperature, and Q is the activation energy for viscous or diffusive motion in the liquid. Similarly, the rate at which atoms leave the crystal is

$$R_M = R_M^\circ \exp\left[-\frac{Q + L_m}{k_B T_{int}}\right], \quad (18)$$

where L_m is the latent heat of fusion. Thus, the activation energy for melting is $Q + L_m$. At equilibrium, the rates for solidification and melting are equal, $R_F = R_M$, and for the interface temperature, $T_{int} = T_m$. Combining (17) and (18):

$$\frac{R_M^\circ}{R_F^\circ} = \exp\left[-\frac{L_m}{k_B T_m}\right]. \quad (19)$$

The velocity of recrystallization [$V_{int}(T_{int}) > 0$] or melting [$V_{int}(T_{int}) < 0$] is given by

$$V_{int}(T_{int}) = R_F - R_M. \quad (20)$$

Utilizing Eqs. (18)–(20), the velocity of resolidification is expressed

$$V_{int}(T_{int}) = C' \exp\left[-\frac{Q}{k_B T_{int}}\right]\left\{1 - \exp\left[-\frac{L_m \Delta T}{k_B T_{int} T_m}\right]\right\}, \quad (21)$$

where

$$C' = R_M^\circ \exp\left[-\frac{L_m}{k_B T_m}\right]; \qquad \Delta T = T_M - T_{int}.$$

Equation (21) can be approximated by a linear relation between the interface velocity and the superheating temperature at the interface:

$$\Delta T = C_3 V_{int}(T_{int}). \quad (22)$$

The material constant C_3, which quantifies the effect of the interface velocity on the superheating temperature ΔT, represents the degree of interface superheating. Kluge and Ray [56] assigned a numerical value to this constant for silicon, $C_3 = 9.8$ K/(m/s), by fitting Eq. (22) to direct molecular dynamics predictions of the interfacial velocity as a function of temperature for epitaxial silicon crystal growth from the liquid phase. This interface response function is adopted in the numerical modeling of rapid melt propagation. In the work of Xu *et al.* [114], the position of the interface and the temperature field were solved by casting Eq. (15), together with the interfacial boundary conditions [Eq. (16)], in an implicit finite-difference form. The solution was iterated to satisfy the response function given by Eq. (22). Direct experimental measurement was recently obtained by Xu *et al.* [113] and will be discussed in the next section.

C. EXPERIMENTAL VERIFICATION OF THE MELTING PROCESS

For comparison with prior published work, we will concentrate on the study of pulsed laser melting of semiconductors in bulk and thin-film form. As will be shown later, certain inherent advantages of specific physical properties of semiconductors allow direct experimental observations. In addition, there are considerable related practical applications, such as annealing of ion implantation surface damage, recrystallization of amorphous and polycrystalline films, and enhancement of dopant diffusion. Both experimental and computational investigations of pulsed laser interactions with semiconductor materials have been performed. Transient conductance measurements [31, 100], nanosecond-resolution X-ray diffraction measurements [64], and time-resolved reflectivity measurements [46] have been applied to obtain quantities such as melt penetration, melt duration, and melt front velocity. The experimental results were

interpreted by numerical simulations to show that the pulsed laser melting of semiconductors in the nanosecond time regime is a thermal phenomenon.

1. Conductance Experiment

Recently Xu *et al.* [114] examined the transient heating and melting of thin polysilicon (p-Si) layers deposited onto fused-quartz wafers by low-pressure chemical vapor deposition (LPCVD), as well as bulk silicon under nonequilibrium conditions. A schematic drawing of the experimental setup is shown in Fig. 1, and the sample configuration is depicted in Fig. 2. The samples are irradiated by a pulsed ultraviolet (UV) KrF excimer laser with wavelength $\lambda = 248$ nm and pulse duration $\tau_p = 52$ ns [full-width half-
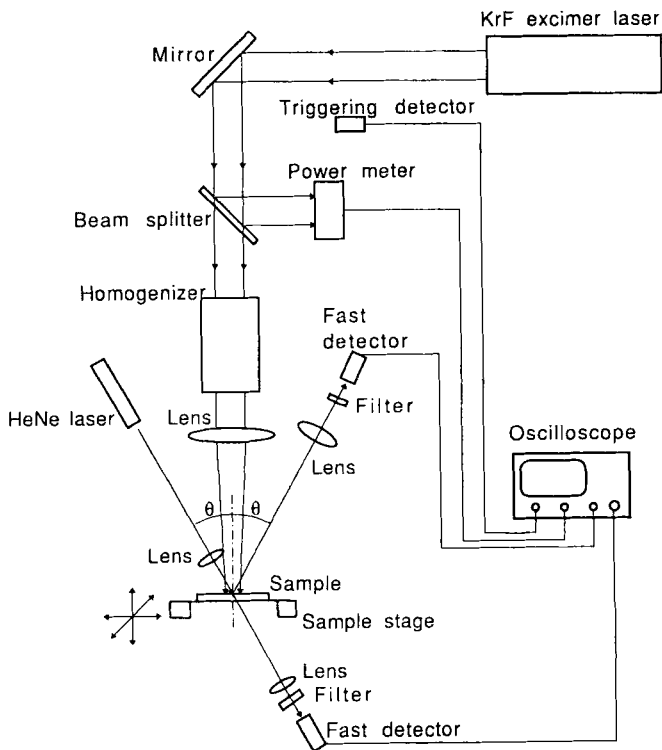

FIG. 1. Experimental setup for optical reflectivity, transmissivity, and electrical conductance measurements during excimer laser melting of polysilicon films ([114], reproduced with permission from ASME).
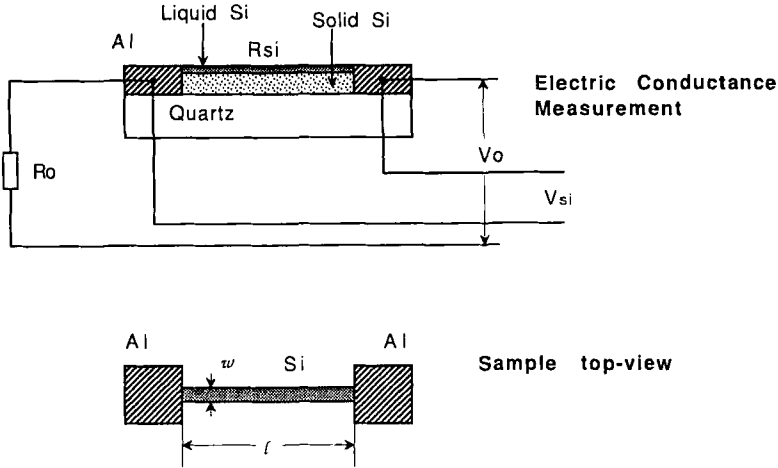
FIG. 2. Sketch of sample and conductance measurement circuit ([114], reproduced with permission from ASME).

maximum (FWHM) = 26 ns]. The interface tracking numerical method was coupled with experimental information to resolve the temperature field and investigate interface superheating. The constant C_3 is taken as 10 K/(m/s) in the calculation, unless noted otherwise.

A continuous-wave (CW) unpolarized HeNe laser (λ = 633 nm) is used as a probing light source for the reflectivity and transmissivity measurement. The resistivity of liquid silicon is lower than that of solid silicon by a factor of five orders of magnitude. When the surface of silicon film starts to melt, the total resistance of the silicon is reduced by several orders of magnitude. The depth of the molten layer can be determined from the transient voltage signal across the p-Si sample when the sample is heated by the pulsed laser. In the transient electric resistance measurement, the photoconductance signal, which is the electric conductance caused by the laser-excited free carriers, could last for microseconds in pure silicon. To reduce the free-carrier lifetime, gold was evaporated on the polysilicon film surface and diffused into the polysilicon film by convective heating. The photoconductance signal in this gold-diffused sample is completely separated from the conductance signal caused by phase change.

Typical transient reflectivity, transmissivity, and conductivity signals are shown in Fig. 3. In Fig. 3a, the laser fluence is just above the melting threshold. Because of the temperature dependence of optical refractive index of silicon at 633-nm wavelength, the reflectivity of solid silicon increases with temperature. The reflectivity reaches 0.73 at about 30 ns
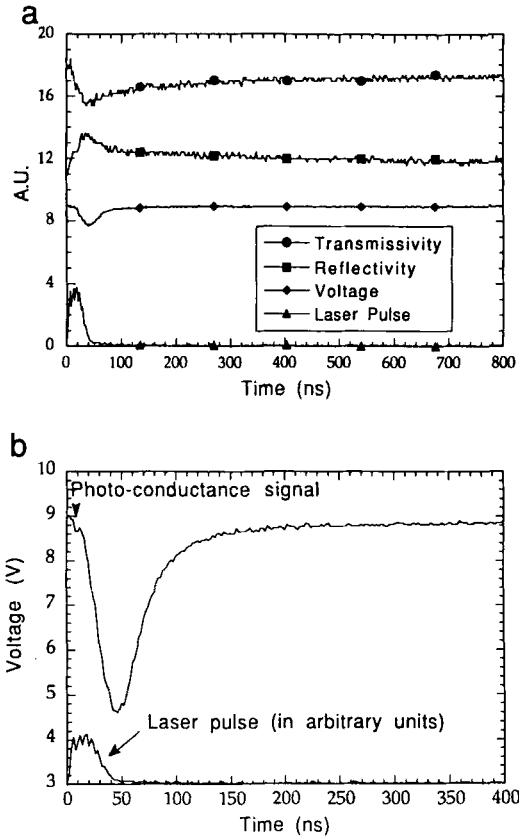
FIG. 3. (a) Reflectivity, transmissivity, and electric conductance signals at a laser fluence slightly above the melting threshold; (b) electric conductance signal at the fluence, $F = 0.32$ J/cm^2 ([114], reproduced with permission from ASME).

when the p-Si is melted. The transition signal decreases when temperature increases and drops to zero when the sample is melted. The electric voltage signal has a photoconductance-induced drop between 0 and 10 ns. The second voltage drop at about 30 ns is due to the melting of the sample surface. In Fig. 3b, the laser fluence is much higher. The initial voltage drop caused by photoconductance lasts about 10 ns. The second voltage drop, which is much larger than the photoconductance signal, is converted to the melt front depth. It is clear that the photoconductance signal is completely separated from the electric signals caused by phase change. Once the p-Si film starts to melt, the total resistance of the film should be

calculated as a liquid film in parallel to a solid film. But since the resistivity of liquid silicon is much lower than that of solid silicon, the resistance of the solid silicon can be neglected. From Fig. 2, the resistance of the film Ω, and the melt depth, δ_m, can be calculated as

$$\Omega_{Si}(t) = \frac{\Omega_0 V_{Si}(t)}{V_0 - V_{Si}(t)}, \tag{23a}$$

$$\delta_m(t) = \frac{l}{w\sigma_{el}\Omega_{Si}(t)}, \tag{23b}$$

where l and w are respectively the length and width of the silicon strip, as shown in Fig. 2. The temperature dependence of the liquid silicon conductivity, σ_{el}, is given by Glazov *et al.* [36].

Figure 4 shows the maximum melting depths at different laser fluences. The melting threshold, determined by both the experiment and calculation, is 0.16 J/cm^2. This value is significantly smaller than the melting threshold of undoped silicon. This is because the reflectance of the Au-doped sample at $\lambda = 248$ nm (0.25) is much lower than that of undoped silicon (0.7 for crystal silicon). At higher fluences, the measured maximum melting depth agrees with the calculated melting depth. Figure 5a shows the melting duration determined by conductance measurement and numerical simulation. The long-lasting "tail" of melting in the transient voltage signal could indicate undercooling, as suggested by Palmer and Marinero [76]. At high fluence ($F > 0.4$ J/cm^2) the measured melting duration is longer than that of the calculated results. This can also be due
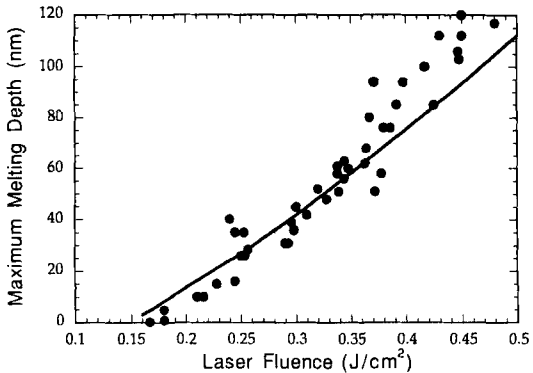

FIG. 4. Comparison between measured and calculated maximum melting depth at different laser fluences ([114], reproduced with permission from ASME).
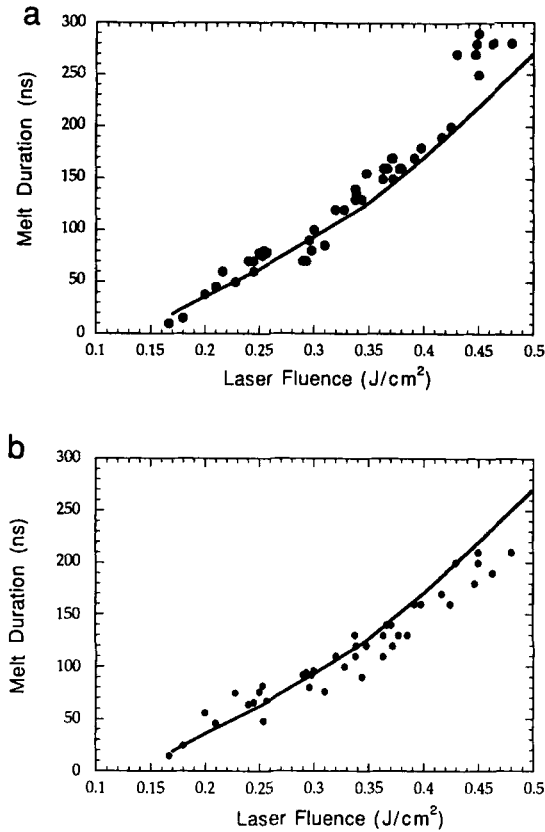
FIG. 5. Comparison between measured and calculated melting duration at different laser fluences. The measured results were determined from (a) electric conductance experiment and (b) transmissivity experiment ([114], reproduced with permission from ASME).

to the liquid undercooling effect. Melting duration can also be determined from transmissivity measurement (Fig. 5b). The melting duration is taken as the time period when the transmissivity stays at zero. This gives a lower value of the melting duration because the penetration depth, d_{ab}, of the liquid silicon at the HeNe laser light wavelength is about 10 nm [91]. When the liquid silicon solidifies to a thickness of less than d_{ab}, the transmissivity starts to rise. The error due to this fact is estimated to be 10%.

Figure 6 compares the transient melting depths with the numerical results at three different laser fluences. The maximum melting depth and the melt duration agree well with the numerical results. The melting and resolidification velocity can be determined from the slope of the melting
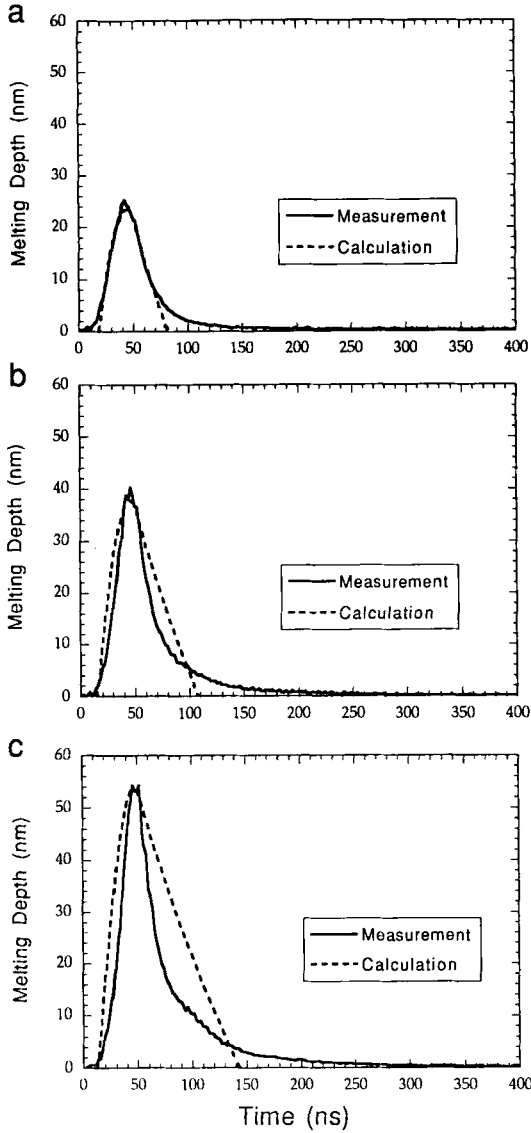
FIG. 6. Comparison between measured and calculated melting depth for different laser fluences: (a) $F = 0.25$ J/cm^2, (b) $F = 0.30$ J/cm^2, (c) $F = 0.35$ J/cm^2 ([114], reproduced with permission from ASME).

front. The maximum resolidification speed determined from Fig. 6 is higher than that of the numerical results. The resolidification speed gradually fades to zero, causing a longer solidification process. It is also apparent that the discrepancies between theoretical predictions and experimental results increase at higher fluences. Meanwhile, the calculated solidification speed is almost constant during the entire solidification process.

The constants can vary due to different microstructure of the material. The effect of different overheating levels on the melting depth and melting duration was examined quantitatively. The transient melting front position at different overheating degrees is shown in Fig. 7a. The coefficient C_3 was varied form 0 (no overheating) to 20 K/(m/s). The predicted melting depths show no significant dependence on overheating levels. The melting durations differ by only about 20 ns from strong overheating to no overheating, whereas the experimental accuracy on determining the melting duration exceeds 20 ns (Fig. 5a, b). On the other hand, the maximum surface temperature rise is higher when there is strong overheating (Fig. 7b).

2. *Pyrometry Experiment*

Another recent experiment by Xu *et al.* [113, 115] has probed the nature of the rapid-phase-change phenomena in undoped p-Si thin films. Surface temperature information is obtained by multiwavelength near-infrared (IR) pyrometry (Fig. 8). The desired temperature range is between 1500 and 3500 K. In this temperature range, thermal emission is strongest at wavelengths between 1 and 2 μm. The major difficulties in fast spectral thermal emission measurements arises from the low signal-to-noise ratio (SNR). Large solid angles are therefore required to achieve sufficient energy collection efficiency. Bandpass filters in the wavelength range from 1.1 to 1.7 μm are used to resolve spectral thermal emission signals at four different wavelengths (1.2, 1.4, 1.5, and 1.6 μm) to enhance the measurement accuracy.

To measure the temperature of the solid–liquid interface during laser melting of the p-Si sample, thermal emission is collected from the *back* side of the sample, as shown in Fig. 9a. In the wavelength range between 1.1 and 1.7 μm, both the solid silicon and the quartz substrate are transparent, so that their emissivity is zero according to Kirchhoff's law. The thermal emission from the solid silicon film and the quartz substrate in this wavelength range is insignificant. However, when the surface of the p-Si film is melted by the pulsed laser beam, the thermal emission from liquid silicon is detectable, since the liquid silicon has an emissivity around
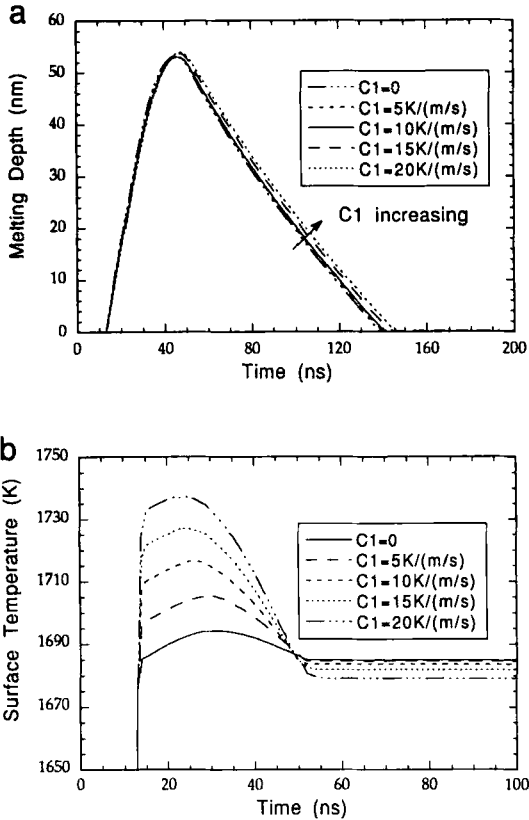
FIG. 7. (a) Calculated melting depth at different superheating levels, $F = 0.35$ J/cm^2; (b) calculated surface temperature at different superheating levels, $F = 0.35$ J/cm^2 ([114], reproduced with permission from ASME).

0.28 in the near-IR. Thus the measured thermal emission signal is ascribed to liquid silicon. At near-IR wavelengths, the radiation absorption depth in liquid silicon is less than 18 nm. Therefore, the thermal radiation is emitted from a thin liquid silicon layer just behind the solid–liquid interface. The temperature derived from the measured thermal emission is close to the solid–liquid interface temperature.

To obtain temperature information from the measured thermal emission, the temperature dependence of the spectral emissivity is required. The emissivity is generally a function of temperature and wavelength. The surface conditions may alter the emissivity drastically. The emissivity of a real sample surface can be much different from the reported literature
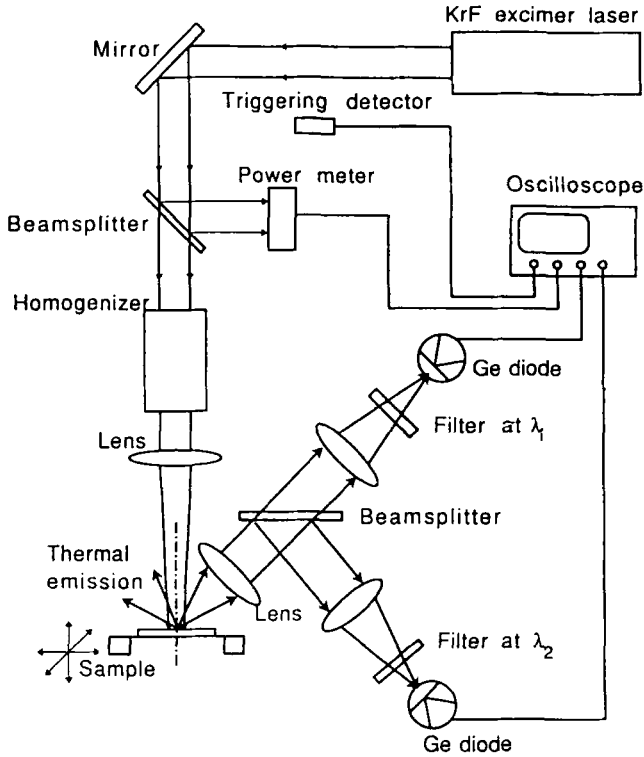
FIG. 8. Experimental setup for transient thermal emission measurement [115].

data for "ideal" surfaces under strictly controlled experimental conditions. In this work, the emissivity of the sample is independently measured. Figure 9b illustrates the experimental setup for measurement of the transient reflectivity during pulsed excimer laser heating. The temporal evolution of the emissivity can be obtained from transient reflectivity measurement. In the transient reflectivity measurement, a quartz halogen (QH) lamp is used as the light source.

The derivation of temperature from thermal emission measurement is based on Planck's blackbody radiation intensity distribution law:

$$e_{\lambda b} = \frac{2\pi C_1}{\lambda^5 \exp(C_2/\lambda T) - 1}, \tag{24}$$

where $e_{\lambda b}$ is blackbody emissive power, λ is wavelength, T is temperature, and C_1 and C_2 are blackbody radiation constants. The strong UV radia-

a

Excimer Laser
Beam

Homogenizer

Lens

Sample   p-Si   film
                                          ← Quartz
                                              substrate

                                              Filter

QH lamp   Ge diode

b

Concave
mirror   Lenses   Monochromator   Pulsed laser
                                                         beam
                                        IR mirror
                                                            Ge diode
Light
source

                                            Θ
                                    Lens   Lenses
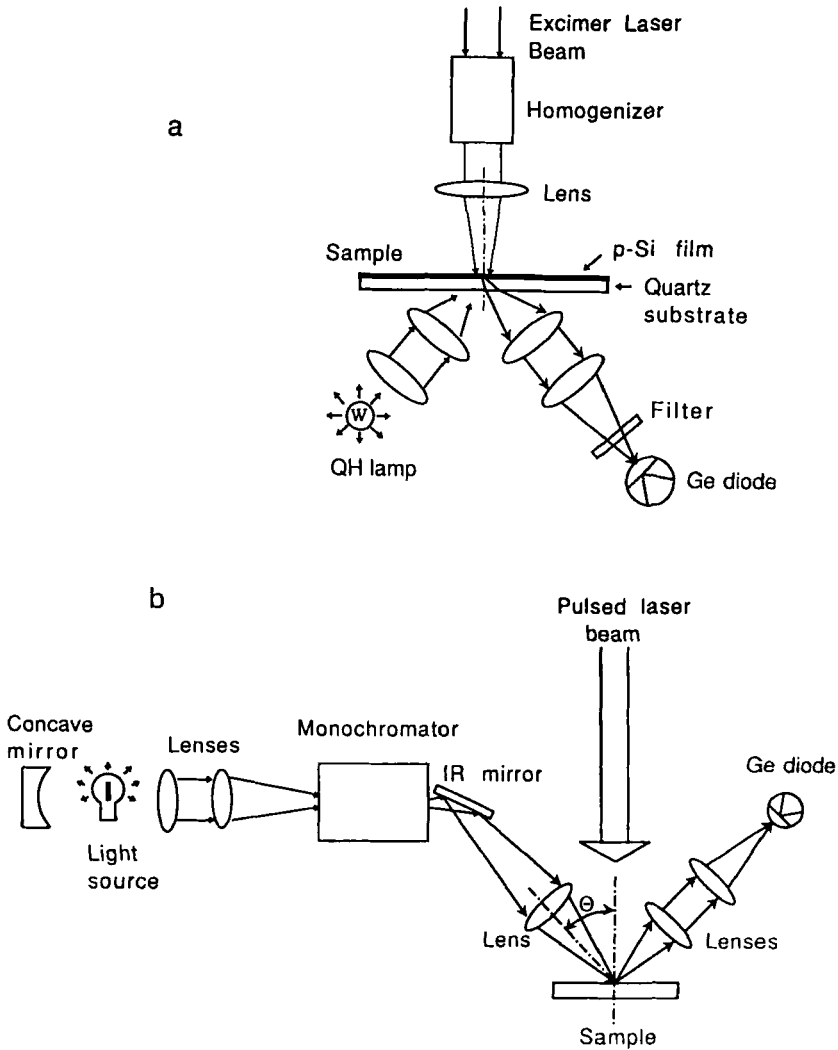
                                          Sample

Fig. 9. Experimental arrangements for (a) interfacial temperature measurement; (b) in situ spectral reflectivity measurement [115].

tion of the excimer laser could trigger the following radiative mechanisms: (1) fluorescence from the optical components and (2) stimulated emission from the sample itself. The effect of the fluorescence in the experiment has been examined and found to be negligible. On the other hand, the stimulated emission from silicon has spectral lines in the UV and visible ranges, well outside the near-IR measurement band.

The detector collects thermal radiation through a solid angle (θ_1 to θ_2, ϕ_1 to ϕ_2) and over a wavelength bandwidth (λ_1 to λ_2). In fact, the voltage signal recorded on the oscilloscope, V, represents an integration of the thermal emission in this solid angle and wavelength band, modified by the emissivity of the material, the transmission of the optical components, and the detector spectral response:

$$V = \Omega/\pi \int_{\lambda_1}^{\lambda_2} \int_{\theta_1}^{\theta_2} \int_{\phi_1}^{\phi_2} \varepsilon_\lambda'(\lambda, \theta, \phi, T) \tau(\lambda) D(\lambda) e_{\lambda b}(\lambda, T) \, d\phi \, d\theta \, d\lambda \, dA,$$

$$(25)$$

where Ω is the impedance of the oscilloscope (50 Ω), $\tau(\lambda)$ is the spectral transmittance of the lenses and filters in the optical path, $D(\lambda)$ is the responsivity of the germanium diode at different wavelengths [in units of amperes per watt (A/W)]; $\varepsilon_\lambda'(\lambda, \theta, \phi, T)$ is the directional spectral emissivity, and dA is the area on the sample that is sensed by the germanium diode.

The emissivity is deduced from transient reflectivity measurement. Invoking Kirchhoff's law, the spectral directional emissivity is equal to the spectral directional absorptivity:

$$\varepsilon_\lambda'(\lambda, \theta, \phi, T) = \alpha_\lambda'(\lambda, \theta, \phi, T). \tag{26}$$

For an opaque, nontransmitting material (such as liquid silicon thicker than ~ 40 nm), the directional spectral absorptivity can be expressed as

$$\alpha_\lambda'(\lambda, \theta, \phi, T) = 1 - R_s'(\lambda, -\theta, \phi, T) - R_d(\lambda, T), \tag{27}$$

where $R_s'(\lambda, -\theta, \phi, T)$ is the specular reflectivity and $R_d(\lambda, T)$ is the diffuse reflectivity. The measured root-mean-square (RMS) surface roughness of the samples used in the experiment was within 50 Å, implying optical smoothness. Also, the melting interface is assumed to be optically smooth. Consequently, it can be argued that the diffuse reflection from the sample surface or the melting interface is negligible compared with the specular reflection. In this case, the emissivity can be expressed as

$$\varepsilon_\lambda'(\lambda, \theta, \phi, T) = 1 - R_s'(\lambda, -\theta, \phi, T). \tag{28}$$

The emissivity is derived using the measured transient reflectivity data in Eq. (28). Once the emissivity is determined and the thermal radiation emission of the target material is measured, the temperature can be obtained by solving Eq. (25). In addition, the effect of a temperature gradient at the solid–liquid interface is considered in deducing the interface temperature. The measured thermal radiation is emitted from a near-interface liquid layer whose thickness is only a few optical absorption depths. Since there exists a falling temperature gradient in the liquid layer toward the melting interface, the temperature assigned to the measured

thermal emission exceeds the interface temperature. Defining the temperature calculated from the thermal emission spectrum as the "effective" temperature, the relation between this effective temperature, T_{eff}, and the temperature distribution inside the liquid film, $T(x)$, is approximated by

$$\int_{\lambda_1}^{\lambda_2} \int_{\theta_1}^{\theta_2} \int_{\phi_1}^{\phi_2} \varepsilon_\lambda'(\lambda, \theta, \phi, T) \tau(\lambda) D(\lambda) e_{\lambda b}(T_{\text{eff}}) \, d\phi \, d\theta \, d\lambda \, dA$$

$$= \frac{1}{d_{\text{ab}}} \int_0^{Nd_{\text{ab}}} \int_{\lambda_1}^{\lambda_2} \int_{\theta_1}^{\theta_2} \int_{\phi_1}^{\phi_2} \varepsilon_\lambda'(\lambda, \theta, \phi, T) \tau(\lambda) D(\lambda) e_{\lambda b}[T(x)]$$

$$\times \exp\left(-\frac{x}{d_{\text{ab}}}\right) d\phi \, d\theta \, d\lambda \, dx \, dA. \tag{29}$$

The left side of Eq. (29) has the form established in Eq. (25). The right side is the measured thermal emission that originates from a liquid layer of thickness equal to a number ($N = 4$) of optical absorption depths (d_{ab}). The x coordinate has its origin at the solid–liquid interface, and is directed into the liquid layer. At the highest laser fluence of 0.95 J/cm^2, the temperature gradient at the interface (about 3.3 K/nm) leads to an overestimation of the measured "effective" temperature by approximately 40 K with respect to the actual interface temperature. It must be pointed out that Eq. (29) does not represent a rigorous solution of the radiative transfer in the skin metal layer, but rather constitutes an approximation to the contribution of the temperature gradient to the aggregate thermal emission. By the same token, in the case of surface temperature measurement, the experimental signal overestimates the actual surface temperature and the same correction procedure is followed. The issue of the internal thermal gradient contributions to the thermal emission warrants further attention, particularly when steep temperature profiles are encountered.

Figure 10 shows the transient thermal $\lambda = 1.5$ μm emission signals measured from the back side of the p-Si/quartz sample at $\lambda = 1.5$ μm for several laser fluences. The thermal emission (and thus the interface temperature) reaches the maximum value several nanoseconds after the initiation of melting. The thermal emission measurement also yields the melting duration, since only liquid silicon emits light in the wavelength range between 1.2 and 1.6 μm. The length of the arrows in Fig. 10 indicates the duration of the melting process at each laser fluence. One interesting feature of the thermal emission signals is the absence of a plateau that would be expected for nearly constant interfacial temperatures. No attempt has been made to extract the transient interfacial temperature; however, it appears that the recrystallization may be driven
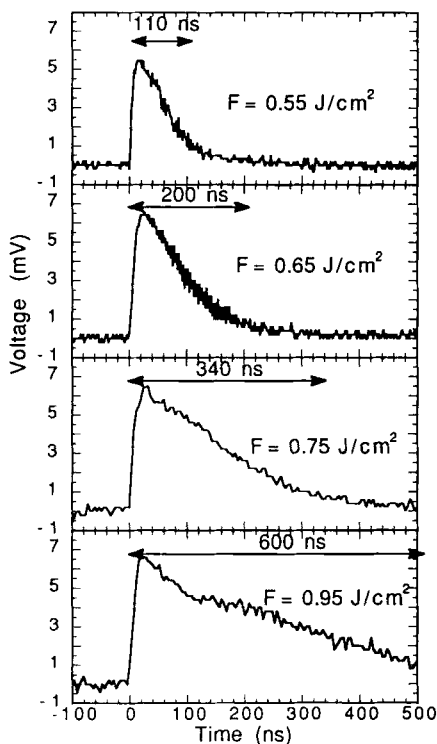
FIG. 10. Thermal emission signals from the back side of the p-Si film at the wavelength $\lambda = 1.5$ μm. The p-Si/quartz sample is heated by excimer laser pulses of different fluences ([113], reproduced with permission from AIP).

by considerable supercooling. Comparing the thermal emission signals at $F = 0.55$ and 0.65 J/cm^2, it can be seen that the maximum interface temperature increases with the laser fluence. However, this trend is not observed for laser fluences higher than 0.65 J/cm^2. The corresponding maximum interface temperatures at different laser fluences are calculated using thermal emission signals at *four* wavelengths. In addition, the effect of a temperature gradient at the solid–liquid interface is considered in deducing the effective interface temperature.

The resulting maximum solid–liquid interface temperatures are shown in Fig. 11a. In Fig. 11b, the melting duration obtained from the thermal emission measurement is compared with the numerical simulation results. Surface optical reflectance probing is employed to independently confirm the melting duration measurement and also examine the possibility that
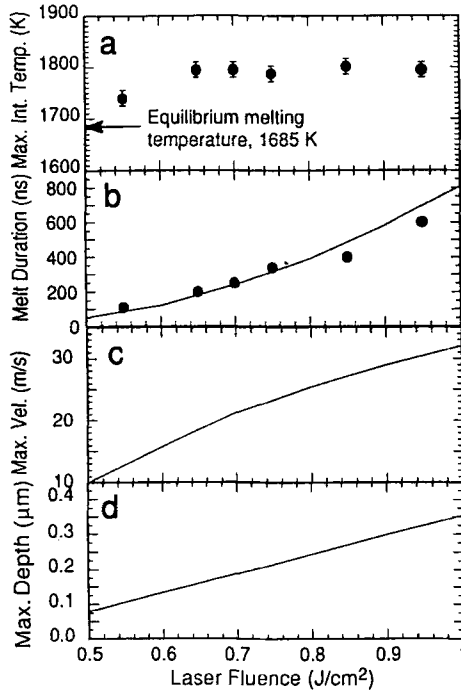
FIG. 11. (a) Maximum melting temperature of the p-Si/quartz sample irradiated by excimer laser pulses of different fluences; (b) comparison between measured and calculated melt durations of the p-Si/quartz sample irradiated by excimer laser pulses of different fluences; (c) calculated maximum melting velocity of the p-Si/quartz sample irradiated by excimer laser pulses of different fluences; (d) calculated maximum melting depth of the p-Si/quartz sample irradiated by excimer laser pulses of different fluences. ([113], reproduced with permission from AIP).

high-temperature solid silicon can contribute to the thermal emission. The surface reflectivity measurement yields the melting duration because of the large increase of silicon reflectance on melting. The surface reflectivity and the back-side thermal emission measurement results are in close agreement. Considering that any thermal emission from high-temperature solid silicon would have to last much longer than the melted phase, the possibility that the back-side thermal radiation is emitted from high-temperature solid silicon is safely dismissed. Figures 11c, d show that the calculated maximum melt front velocities and maximum melting depths increase with the excimer laser fluence. Numerical calculation also predicted that the maximum surface temperature does not reach the evapora-

tion temperature (2628 K) at the highest laser fluence used in the experiment. The relation between the interface velocity and the interface superheating temperature allows determination of the interface response function during the laser-induced melting process. The melting velocity achieved is on the order of tens of meters per second, suggesting a departure from equilibrium conditions. The measured interface superheating temperature combined with the calculated interface velocity provides an experimental study of the interface kinetics under high-power laser irradiation. Assuming that there is a linear relation between the interface superheating temperature and the interface velocity at fluences lower than 0.65 J/cm^2 (more properly, when the interface velocity is below 20 m/s), the response function coefficient C_3 is determined to be about 6 K/(m/s). However, a constant interface temperature is measured at laser fluences higher than 0.65 J/cm^2. The linear interface response function is therefore invalid in the high-laser-fluence regime. When the interface velocity is higher than 20 m/s, the interface superheating temperature is "saturated" at about 110 K.

The measured transient surface temperature of a bulk-Si sample irradiated by an excimer laser pulse at the fluence, $F = 0.9$ J/cm^2, is shown in Fig. 12. Also shown in this figure is the calculated surface temperature at the same laser fluence. The effect of superheating is illustrated in the calculation. The material constant C_3 is taken as 6 K/(m/s), which is the measured value for the polycrystalline silicon samples. For comparison, the calculation results without considering superheating are also shown in Fig. 12. Compared with the calculated results, the measured maximum surface temperature is higher, and a longer time is needed to reach the
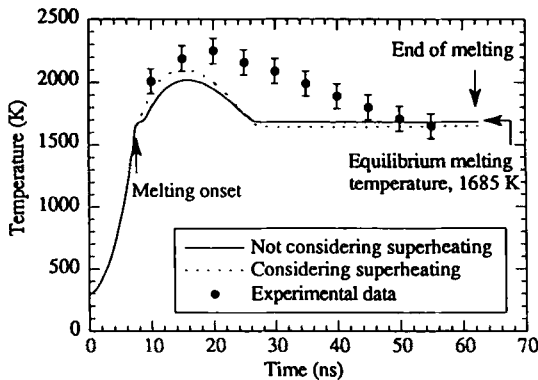

FIG. 12. Measured and calculated surface temperature histories during melting of a bulk, crystalline Si sample with an excimer laser pulse of fluence $F = 0.9$ J/cm^2.

highest surface temperature. The discrepancy could result from a higher superheating surface temperature for single-crystal Si (c-Si). It is worth noting that Boneberg *et al.* [12] examined the variation of the optical reflectivity of a c-Si wafer during irradiation with two successive frequency-doubled neodymium: yttrium aluminum garnet (Nd: YAG) (λ = 532 nm) laser pulses of nanosecond duration. The first pulse melted the surface, increasing the reflection coefficient up to the value of the metallic liquid silicon. On further heating of the surface with a second, time-delayed pulse, a decrease of the reflection coefficient was observed by up to 9% at the probing HeNe wavelength (λ = 633 nm), resulting from the temperature-dependent dielectric function of molten silicon.

Knowledge of the temperature field is essential for studying in detail the phase transformation mechanisms of pulsed-laser-induced amorphization and recrystallization of silicon films on SiO_2 substrates [14, 42, 85]. The critical issue is the degree of supercooling driving the rapid solidification.

D. ULTRASHALLOW p^+-JUNCTION FORMATION IN SILICON BY EXCIMER LASER DOPING

Control of the temperature field and the melt depth can lead to formation of box-shaped ultrashallow doping profiles in semiconductors. Excimer-laser-driven doping from the gas phase has been demonstrated by Landi *et al.* [63] and Matsumoto *et al.* [68]. Promising results have been reported recently using a simple excimer-laser-induced method from a spin-coated dopant solid glass layer [117]. The c-Si wafer is coated with a boron-doped spin-on-glass layer of 3000-Å thickness. Rapid boron diffusion in the liquid silicon is achieved during melting; however, on the contrary, the diffusion is limited by the phase boundary during the solidification process.

In order to understand the heat and the mass transfer in the ultrashallow p^+-junction formation under the excimer laser irradiation on the silicon wafer with a thin solid diffusion oxide film, a one-dimensional numerical analysis is developed to simulate the transient heat and mass diffusion of the boron atoms across the thin molten silicon layer. As a first-order approximation, the thermal properties are independent of the concentration and the mass diffusivity is independent of the temperature. Therefore, the mass diffusion is decoupled from the thermal equations. The heat transfer is treated using the enthalpy scheme discussed in Section I.B. The mass diffusion is solved numerically at each step after the temperature field and the melt–solid interface location are found. Transient boron mass diffusion in this work is modeled by the one-dimensional

Fick's equation:

$$\frac{\partial C}{\partial t} = \frac{\partial}{\partial x}\left(D\,\frac{\partial C}{\partial x}\right). \tag{30}$$

The boundary conditions and the initial condition for the mass transport are given:

$$C(x=0,t) = C_0, \qquad C(x=d_{ss},t) = 0, \qquad C(x,t=0) = 0, \tag{31}$$

where the surface boron concentration C_0 is chosen as the experimental value. The boron diffusivity D is set as a constant 2.3×10^{-4} cm^2/s in liquid silicon [58] and zero is solid, due to the six orders of magnitude difference between the mass diffusivities in the two phases. The boron dopant concentration profiles are measured by secondary-ion mass spectrometry (SIMS) [106]. The profile obtained at a fixed excimer laser pulse fluence of 700 mJ/cm^2 are shown in Fig. 13; p$^+$ junctions with depth of 70 nm to 140 nm are successfully fabricated, and the boron concentration as high as 2×10^{20} atoms/cm^3 is obtained. This value is about the boron solubility in crystalline silicon. Such a high doping level is due mainly to the high boron mass diffusivity in the thin liquid silicon layer induced
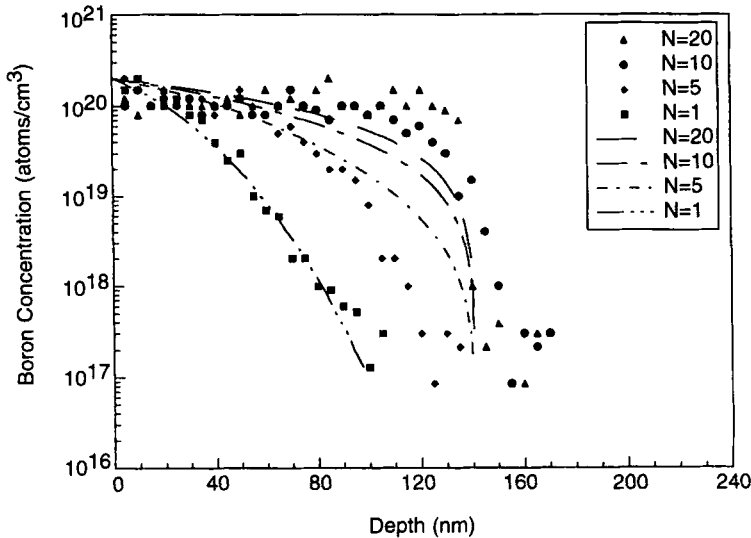

FIG. 13. Ultrashallow p$^+$-junction dopant concentration depth profiles at different laser pulse numbers N with a fixed laser fluence of 0.7 J/cm^2. The solid dots represent experimental data measured by the second ion mass spectroscopy (SIMS) and the lines are numerical results [117].

by the pulsed laser irradiation. The diffusion profiles are driven deeper
into the thin molten silicon as the laser pulse number increases, although
the highest concentration limit is the boron solubility. It is interesting that,
as the laser pulse number increases, the dopant profile shape is more
"box-like" rather then the gradual decrease observed in most diffusion
cases. The abrupt or box-like dopant profiles render the ideal p^+-junction
properties [105]. The art in the information of this box-like shape lies on
the fact that, as the pulse number increases, the boron diffusion is limited
by the maximum melting depth determined by the pulsed laser energy and
pulse width. After the boron diffusion reaches the maximum melting
depth, more boron atoms accumulate in the molten layer instead of
crossing the melt–solid interface, because of the very low boron diffusivity
in the solid silicon. At 20 laser pulses, almost the entire thin molten layer
of 140-nm thickness is saturated with boron dopant. It is also demon-
strated that the p^+-junction depth can be incrementally changed by varying
the laser pulse number at a fixed laser fluence. Numerical simulation
based on the one-dimensional transient thermal and mass diffusion model
predicts similar p^+-junction profiles. Both the experimental and numerical
dopant profiles at larger pulse numbers coincide to a certain depth about
140 nm, the maximum melting depth. The computational results fit the
experimental profile well for the first laser pulse, but deviate substantially
as the pulse number N increases. Numerically predicted dopant concentra-
tions are generally lower than the experimental ones. It is believed that the
boron diffusivity may depend on the boron concentration if the region is
heavily doped, compared with the silicon intrinsic carrier of the order of
10^{19} cm^{-3} at the melting temperature [107]. For the first few pulses, the
heavily doped region is so small that the effect from the concentration
dependence of the boron diffusivity is not significant. Boron diffusivity can
be treated as a constant in the computations. As the pulse number
increases, a larger fraction of the molten region becomes heavily doped,
leading to a change in the boron diffusivity. A larger boron diffusivity
could result in higher computed concentration for $N = 10$ and $N = 20$ in
Fig. 13. There are other factors possibly causing the differences between
the experimental profiles and numerical profiles at higher pulse numbers.
The measured laser fluence is averaged over the pulses for the case of
multipulse laser irradiation. Pulse-to-pulse fluence fluctuations generated
by the excimer laser can be as large as 10%. The fluctuations can result in
not only changes in the thermal process but also in the mass diffusion. The
final dopant profiles are affected more strongly by the higher fluence
pulses than the lower ones during the multipulse doping. Second, the
microstructure in the resolidified thin layer is also of importance during
the multipulse laser irradiation. Assuming epitaxial recrystallization in the

thin liquid silicon layer, the numerical simulation in this work may not be accurate enough to predict the thermal transport because of possible changes in physical properties such as the thermal diffusivity in the recrystallized silicon. Finally, the thermal conductivity of solid silicon layer can be decreased by a factor of 2–5 in the temperature range from room temperature to 600 K because of the heavy doping with boron [95, 98]. At higher temperature, the thermal conductivity becomes less affected by the high dopant concentration. The decrease in thermal conductivity can lead to deeper and longer melting in silicon. The 10% increase in the liquid silicon thermal conductivity from 1685 to 1980 K during the pulsed laser doping may also influence the transient thermal and mass transport [111].

Figure 14 shows boron dopant depth profiles for different laser fluences at a fixed pulse number $N = 20$. It is demonstrated that the p^+ junctions are box-like for 0.6, 0.7, and 0.8 J/cm^2, but not for 0.9 J/cm^2. The difference can be explained by the maximum melting depth. For the fixed pulse number $N = 20$, the boron diffusion depths already exceed the maximum melting depth at the laser fluences 0.6, 0.7, and 0.8 J/cm^2. The accumulation of the dopant atoms is blocked by the liquid–solid interface
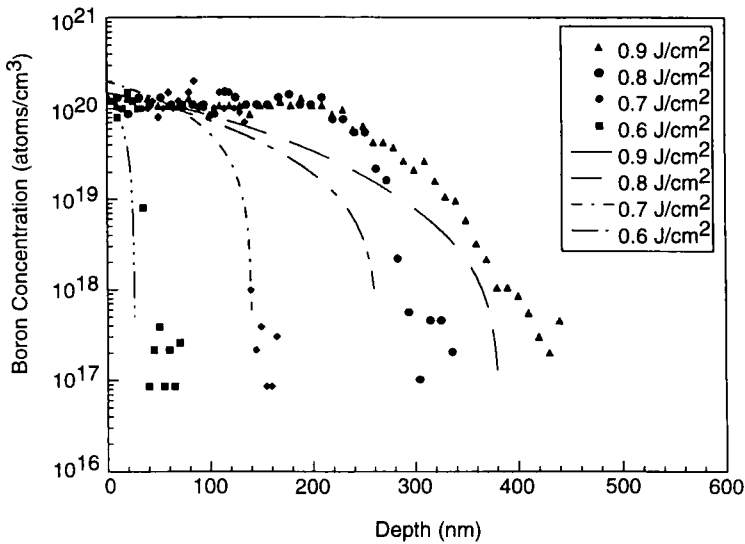

FIG. 14. Ultrashallow p^+-junction dopant concentration depth profiles at different laser fluences with a fixed pulse number $N = 20$. The solid dots represent experimental data measured by SIMS, and the lines are numerical results [117].

and results in the box-like dopant distributions. However, for higher laser fluences such as 0.9 J/cm^2, the diffusion length at $N = 20$ is smaller than the maximum melting length, and therefore, no dopant accumulation occurs. The p$^+$-junction depth increases with the laser fluence because of the increase in both the melting depth and the melting duration. By defining the p$^+$-junction depth d_j as the distance from the surface to the position where the concentration drops below 10^{18} cm^{-3}, the dependence of the junction depth versus the laser fluence is shown in Fig. 15 for two different pulse numbers, $N = 1$ and $N = 20$. The computed junction depths are plotted for comparison. Gradual saturation of the junction depths with the pulse number N at fixed laser fluences is observed in Fig. 16, implying melt–solid interface-limited diffusion. The ultrashallow p$^+$ junctions of 30-nm depth at laser fluence 0.6 J/cm^2 are successfully fabricated with this spin-on-glass (SOG) pulsed laser doping technique. It is demonstrated that the incremental depth achieved by varying the pulse number N can be as small as 20–30 nm. However, the incremental depth achieved by varying the laser fluence at an experimentally controllable level (about 0.1 J/cm^2) is larger than that obtained by varying the pulse number. This is because the melt depth is mainly dominated by the larger
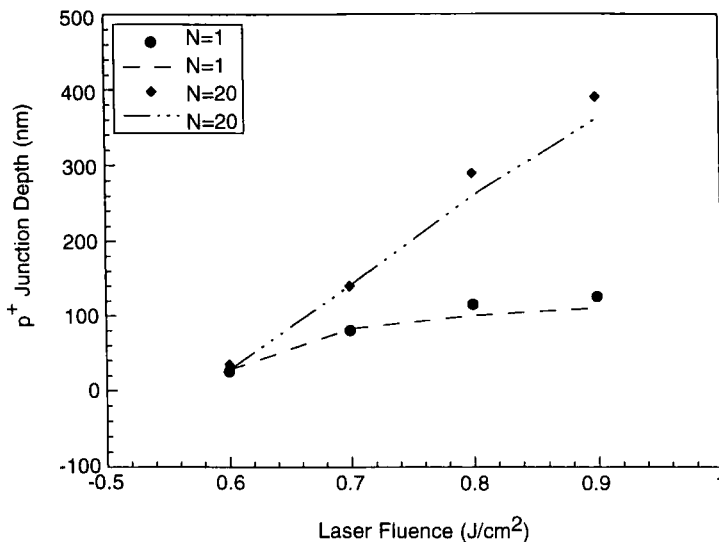

FIG. 15. Ultrashallow p$^+$-junction depth dependence on the laser fluence for $N = 1$ and $N = 20$. The solid dots indicate experimental data measured by SIMS, and the lines show numerical results [117].
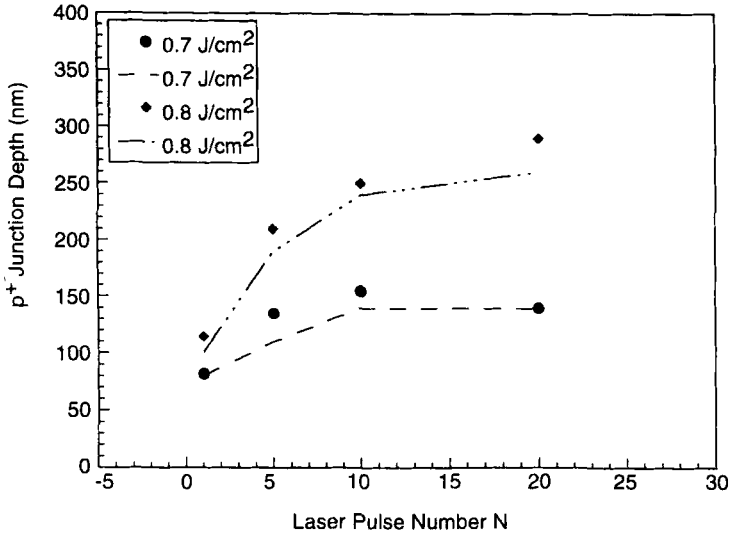
FIG. 16. Ultrashallow p$^+$-junction depth dependence on the laser pulse number for laser fluences 0.7 and 0.8 J/cm^2. The solid dots represent experimental data measured by SIMS and the lines, numerical results, [117].

melting depth and melting duration. The p$^+$-junction sharpness is an important factor in the device performance. By defining the relative junction sharpness as $d_j/\Delta d_j$, where Δd_j is the junction transition depth, it is found that the p$^+$-junction sharpness increases rapidly as the pulse number N increases for the lower laser fluences of 0.6, 0.7, and 0.8 J/cm^2, as shown in Fig. 17. For the laser fluence of 0.9 J/cm^2, the p$^+$-junction sharpness grows much slower than the lower fluence cases because the melting depth is longer than the diffusion depth up to 20 pulses, as mentioned earlier. Again, the melt–solid interface-limited diffusion is confirmed in Fig. 17. The optimal fluence range in pulsed laser SOG doping is therefore positioned at about 0.6–0.8 J/cm^2. The transient pulsed laser induced melting and diffusion in silicon is a complex phenomenon. Many factors, especially the physical properties of this silicon layer, can be altered during the multiple laser pulses. It should be pointed out that the boron diffusivity dependence on the concentration and the temperature in the thin liquid silicon layer is not known yet.

E. TOPOGRAPHY FORMATION

In the studies of pulsed laser melting of silicon described in the previous two sections, the irradiated surface did not produce pronounced topo-
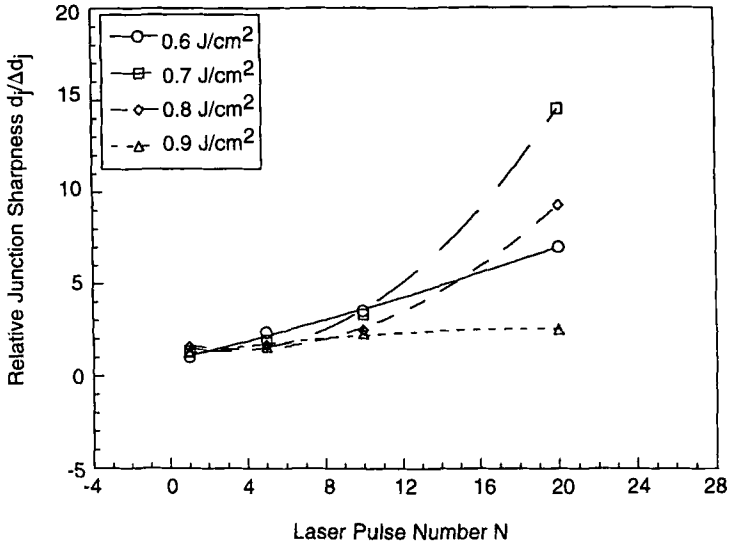
FIG. 17. Relative p^+-junction sharpness dependence on the laser pulse number at laser fluences as 0.6, 0.7, 0.8, 0.9 J/cm^2 [117].

graphic features on the completion of the resolidification process. In those experiments, the semiconductor material was subjected to irradiation by a single pulse, or a limited number of pulses. It is known, however, that periodic wave structures may be induced by laser irradiation on the surface of semiconductors, metals, polymers, dielectric materials, and liquids. This phenomenon was observed for a variety of laser beam parameters, ranging from continuous-wave (CW) beams or Q-switched pulses at intensities even below the damage threshold for some materials to picosecond pulses [28] and femtosecond UV pulses [37]. A theory explaining periodic patterns scaling with the incident laser light wavelength based on the concept of radiation "remnants" scattered from irregular surface structures was proposed by Sipe *et al.* [94] and Young *et al.* [112]. Other studies attributed the formation of surface structures of periods longer than the incident laser light wavelength to melt flow instabilities. Tokarev and Konov [99] presented a theoretical study of thermocapillary waves induced by surface shear stress variations in laser melting of metals and semiconductors. It has also been hypoythesized that thermoelectric body forces exerted on melted semiconductors can also be destabilizing [24]. On metals, studies of target topography have shown formation of columnar structures [61, 62, 71], which have been observed to roughly align coaxially with the incident laser beam. The interrelation between melting, topography formation, and

sputtering mechanisms in excimer laser melting of gold was examined by Bennett *et al.* [9]. Gold was selected as a model system, because it does not introduce oxidation, which would alter the surface characteristics.

Figure 18a–d show the influence of the laser beam angle of incidence on steady-state surface topography on a gold target. The surface droplet formations are seen to increase as the laser beam angle of incidence decreases. There is very little ridge formation at angles close to 0°, but as the laser beam angle of incidence increases, ridge formation evolves—first almost in a parallel pattern, then becoming more chaotic at larger angles of incidence. The laser fluence was maintained at 1 J/cm^2 in this sequence, and topographies represent steady-state conditions. Figure 19 shows in more detail under higher magnification the surface feature formations for a 5° angle of laser beam incidence. This micrograph shows that the nearly spherical droplets have a radius of 1 μm and are arranged in a regular square pattern with a characteristic spacing of about 4 μm. In addition, a visual examination of the ablation surface showed that as the laser fluence increased, so did the presence of surface topographies.

At least four important effects of surface topography on the ablation process can be recognized: (1) the roughening of the surface provides greater surface area for molecular flux leaving the surface, (2) roughened surface topography supports surface droplet formation, (3) surface roughening will enhance the net laser to surface energy coupling by introducing multiple reflections, and (4) the surface topography may enhance local radiative heating, for example, in "valley" formations, due to surface reflections. Two possible mechanisms affecting topographic development are instability waves in the transiently existing thin melt and locally enhanced radiation heating and/or shadowing coupled to thermocapillary forces.

In a laser ablation process, the formation and hydrodynamic removal of large droplets increases the net material removal rate. However, the introduction of droplets into the ablation plume becomes undesirable when sputtering thin films, and is one of the principal disadvantages in using laser ablation for deposition of thin metal films. Past research has established connections between the droplet density and such factors as surface topography [70], target material density [87], laser fluence and laser intensity homogeneity [88], laser angle of incidence [101], and incident radiation wavelength [59]. Van de Riet *et al.* [101] demonstrated a 10 fold reduction, by percent volume, in droplet production, accompanied by a reduction in droplet size, when the ablation target was scanned continuously to provide a virgin surface for the ablation process. Additionally, they showed that the volume percent of droplet production decreased, surprisingly, as the fluence increased for a scanning ablation process.
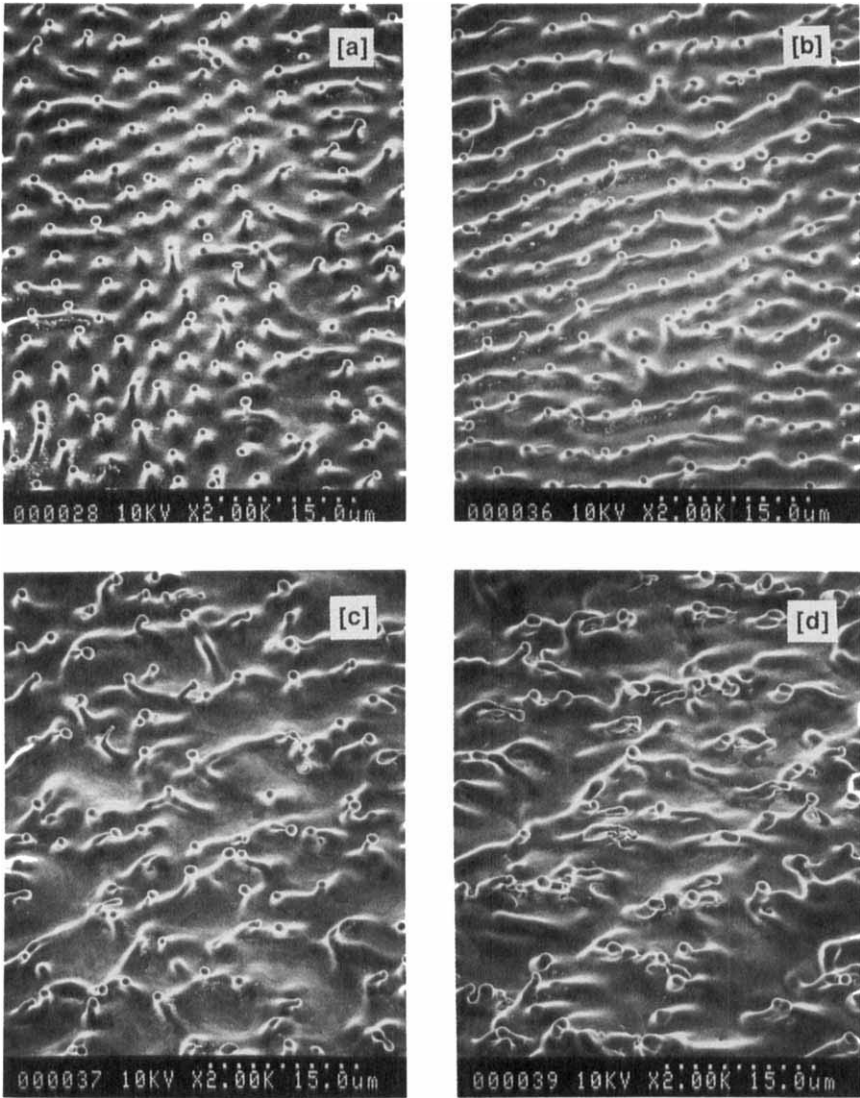
FIG. 18. Scanning electron micrographs showing the influence of the laser beam angle of incidence on the steady-state surface topography at a constant excimer laser fluence $F = 1$ J/cm^2: (a) $\theta_i = 5°$ produces an abundance of droplets with reduced ridge formations; (b) $\theta_i = 15°$ produces highly columnar ridge formations; (c) for $\theta_i = 25°$, a reduction in the number of droplets and loss of ridge columns is observed; (d) $\theta_i = 45°$ produces higher surface agitation with reduced number of droplets ([9], reproduced with permission from AIP).
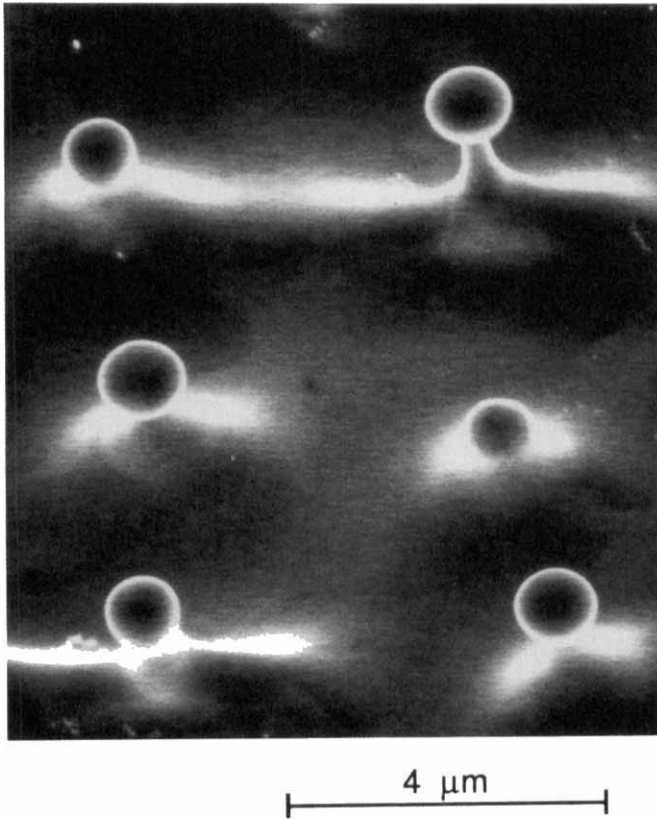
FIG. 19. High-magnification scanning electron micrograph image of surface droplets shown in Fig. 18a ($F = 1$ J/cm^2, $\theta_i = 5°$) demonstrating characteristic length scales for droplet growth ([9], reproduced with permission from AIP).

Some of the characteristics of the ablation plume, including droplet production, were investigated by sputtering a thin film. The measurement of the thin-film thickness distribution determined that the ablation plume peaks at 12° off-axis from the normal and in the direction of the incident laser beam. The surface topography is indeed responsible for "deflecting" the plume. However, the deflection simply reflects a net change in the mean normal direction of surface area contributing to the ablation flux. The angular yield distribution is found to be highly forward-peaking, approximately fitting a cos^{16} θ' curve where the angle θ' is measured from the centerline of the plume instead of the normal to the target surface. It has been suggested that strong forward-peaking plumes could indicate that

the molecular flux from the ablation surface is not liberated as "freely" as the classic evaporation model assumes [13].

The percentage of material in the ablation plume made up of large droplets was also estimated. Kelly and Rothenberg [51] suggested that the majority of metallic material removed by laser ablation detaches hydrodynamically as droplets. However, from a survey of SEM pictures of the sputtered gold film it was recently concluded [9] that less than 10% of the bulk film deposited consisted of micrometer-size droplets. This study of the gold film deposition revealed that droplets around 1 μm in diameter were most preferentially liberated from the surface. Also, no significant change in percent volume of droplet present on the deposition was found as the film was surveyed radially outward from the peak.

In order to develop a comprehensive description of the laser sputtering, some idea of the transient thermal conditions of the target is required. A one-dimensional model of the transient heat transfer with phase change in a gold target has been formulated [9] using the previously discussed enthalpy model. As argued before, the laser beam spot size is two orders of magnitude greater than the thermal penetration depth, suggesting that the surface conduction of heat is one-dimensional. Nevertheless, the one-dimensional modeling of the surface ablation process is recognized as a simplification of surface conditions that arise over the course of many irradiation pulses. Despite the flat initial condition of the ablation target, experimental observations demonstrate topographic development of the target over several hundred laser pulses, which diminishes the assumed one-dimensional geometry. Consequently, the development of one-dimensional effects in the heat conduction and the local surface irradiation represent the most significant shortcoming of the model. However, the one-dimensional model provides sufficient insight into the thermal condition of the target to warrant its consideration.

Results of the numerical model are presented in Fig. 20 for the laser fluence $F = 1$ J/cm^2. Of specific concern are the thermal penetration depth in the target solid δ_T, the melting depth δ_m, the melting duration τ_m, and acceleration of the liquid–solid interface in the target a_{int}. During most of the period in which the surface melt exists, the acceleration of the liquid/solid interface is found to be $|a_{int}| = 4.6 \times 10^9$ m/s^2, and is in the direction pointing outward normal to the target surface.

Inertial forces acting on the melt are responsible for development of surface topography. Two effects lead to acceleration of the surface melt. The first effect is a direct consequence of phase change, when the densities of the liquid and solid are not equal. The second effect arises from the thermal expansion of the target material. The time scale for mechanical
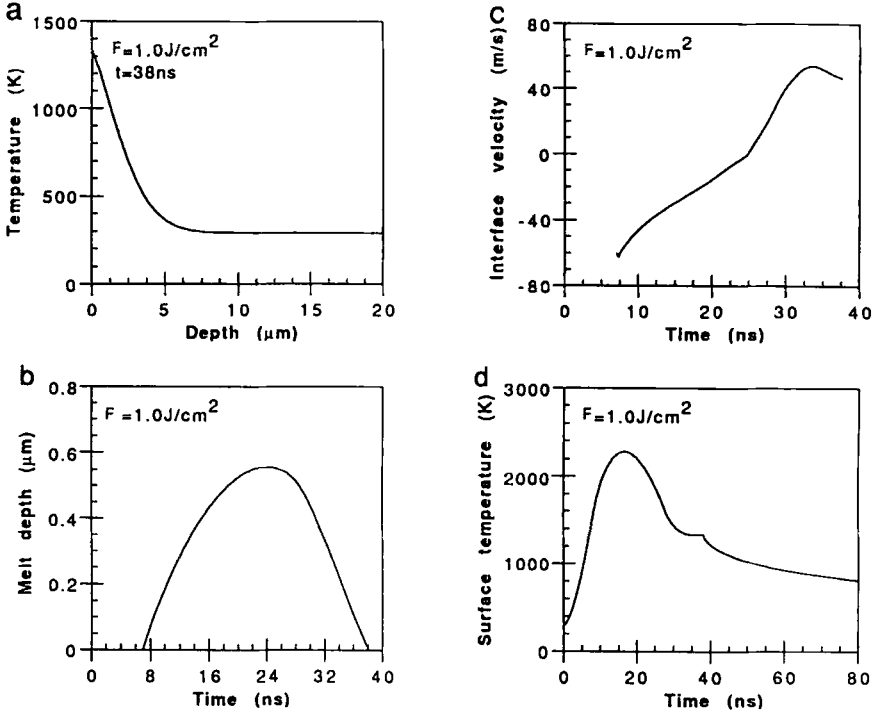
a 1500

$F=1.0J/cm^2$
$t=38ns$

Temperature (K)

1000

500

0

0   5   10   15   20
Depth (μm)

c 80

$F=1.0J/cm^2$

Interface velocity (m/s)

40

0

-40

-80

0   10   20   30   40
Time (ns)

b 0.8

$F=1.0J/cm^2$

Melt depth (μm)

0.6

0.4

0.2

0

0   8   16   24   32   40
Time (ns)

d 3000

$F=1.0J/cm^2$

Surface temperature (K)

2000

1000

0

0   20   40   60   80
Time (ns)

FIG. 20. Numerically calculated thermal conditions of the gold target during sputtering at $F = 1$ J/cm²: (a) temperature spatial distribution in the target on completion of melt resolidification; (b) surface temperature temporal behavior; (c) melt depth temporal behavior; (d) liquid–solid interface velocity behavior ([9], reproduced with permission from AIP).

expansion of the solid target, τ_{mech}, is evaluated with respect to the thermal penetration depth ($\delta_T (\sim 5$ μm) and the propagation velocity of dilatational waves v_e (3200 m/s) in the target solid. It is determined that τ_{mech} is an order of magnitude smaller than the melting duration τ_m:

$$\tau_{mech} = \frac{\delta_T}{v_e} \sim 2 \text{ ns} < \tau_m = 31 \text{ ns.} \qquad (32)$$

From this observation, it is arguable that, due to the relatively short time scale of expansion, the target expands nearly to the extent it would if thermal conditions occurred "quasi-statically." Within this approximation, it follows that thermal expansion is prescribed by a knowledge of the temperature field (and the linear expansion coefficient) in the target

material. It is therefore asserted that

$$|a_{m,t}| \sim \alpha_{th} \Delta T_p / \delta_T(\tau_m)^2 = 5 \times 10^7 \text{ m/s}^2 \tag{33}$$

represents an order-of-magnitude estimate of the acceleration experienced by the melt due to thermal expansion of the target solid. In Eq. (33), ΔT_p (520 K) represents an average rise in temperature over the thermal penetration depth δ_T (5 μm) occurring within the time scale of the melt duration τ_m (31 ns). In ascertaining the melt acceleration due to phase change, it will be assumed that the acceleration discontinuity at the interface is "communicated" rapidly throughout the liquid (2500 m/s) with nearly the same velocity as through the solid. Melt acceleration due to phase change is related to the liquid/solid density ratio ($\rho_s/\rho_l = 1.055$) at the melting temperature, as well as the local acceleration of the liquid–solid interface, a_{int}. By invoking mass conservation across the liquid–solid interface, we can estimate the melt acceleration due to phase change as

$$a_{m,p} \sim a_{int}\left(1 - \frac{\rho_s}{\rho_l}\right)_{int} = 2.5 \times 10^8 \text{ m/s}^2. \tag{34}$$

Since acceleration of the melt resulting from thermal expansion is an order of magnitude smaller than that resulting from phase change, the former can be neglected. Therefore it is estimated that the melt is accelerated toward the target with an acceleration of the order of magnitude

$$|a_m| \sim 2.5 \times 10^8 \text{ m/s}^2. \tag{35}$$

The spatial distribution between surface droplets demonstrated for normal incident irradiation is governed by instability at the melt surface. Because of the change in density occurring during phase change, the acceleration of the liquid–solid interface (during both melting and resolidification) accelerates the surface melt and imposes an inertial force from the body of the melt. Since acceleration of the melt is into the target, the apparent body force experienced by the melt is directed away from the target. The inertial force is destabilizing the melt surface. Surface tension, however, is stabilizing and exerts a force that attempts to maintain a flat surface. The instability of an interface between two phases is a typical problem that has been treated for more general conditions than will be required here [17]. The instability arising from a motionless liquid overlaying a motionless vapor, in the presence of a gravity field, is known as a *Rayleigh–Taylor instability*. The instability experienced by the melt is also Rayleigh–Taylor, since in the reference frame of the melt, the inertial force due to acceleration acts as a gravitational body force.

The initially flat interface is subjected to spatially periodic disturbances. The wavelength of the disturbance that grows most rapidly is termed "the most dangerous wavelength." For the conditions of the surface melt, it is found that the most dangerous wavelength is

$$\lambda_D \sim 2\pi \left(\frac{3\sigma}{\rho_l |a_m|} \right)^{1/2} \sim 5.0 \ \mu\text{m}, \tag{36}$$

which agrees remarkably well with the periodicity demonstrated by droplet growth on the target surface, as seen in Fig. 19. If on the other hand, the relative magnitudes of liquid and solid densities are reversed (i.e., $\rho_s < \rho_l$), the melt would experience a restraining body force back into the target, and there would be no destabilizing event to sponsor topographic growth. Silicon has a liquid density greater than the solid and produces no topographies comparable to the gold target on irradiation with excimer laser pulses. To estimate the requirement leading to the formation of a droplet than can ultimately be liberated from the surface, the forming droplet is modeled as a hemispheric dome. If the inertial force acting on the hemisphere is greater than the restraining force, the droplet will grow. This condition implies that

$$D_d \sim \sqrt{\frac{12\sigma}{\rho_l |a_m|}} \sim 1.6 \ \mu\text{m}. \tag{37}$$

This dimension is higher than the diameter of droplets seen on the surface of the target. This discrepancy may indicate that the melt experiences an acceleration even greater than originally calculated. The agreement obtained by invoking this simple stability analysis is remarkable, but has to be viewed considering the assumptions made: perfect initial surface flatness, and no contamination modifying the surface characteristics. It is also conceivable that other modes of instability may appear in the thin melt film.

II. Pulsed Laser Sputtering of Metals

A. BACKGROUND

Many mechanisms contributing to the net surface material removal rate have been identified with the laser ablation process. References to "thermal" or "photothermal" surface ablation in the literature generally embrace a model in which, on absorption, laser light energy is converted to lattice vibrational energy before bond breaking liberates material from the

bulk surface. The thermal mechanism is distinct from a "photochemical" or "electronic" process in which laser-induced electronic excitations lead directly to bond breaking before an electronic-to-vibrational energy transition has occurred. Both thermal and electronic ablation mechanisms liberate molecular size material from the surface, and either one or the other (or possibly both) are likely to be present to some degree in all laser ablation systems. This is distinct from two other ablation mechanisms, identified in the literature as hydrodynamic ablation and exfoliation, which lead to the introduction of large clusters, fragments, or droplets into the ablation plume. The "hydrodynamic" mechanism refers to the formation and liberation of micrometer-size droplets from the melt at the surface. The term *hydrodynamic* arises from the belief that bulk motion of the melted material is involved in the formation and ejection of droplets. *Exfoliation*, on the other hand, refers to an erosion-like mechanism by which bulk material is removed from the surface as an intact solid "flake." Separation of the flake from the surface is thought to occur along energy-absorbing defects in the material.

Kelly and Rothenberg [51] estimated that thermal evaporation could account for less than 1% of the total material removed, and concluded that hydrodynamic sputtering must account for the remainder. Regardless of the presence of hydrodynamic sputtering, first-order principles demand that the accumulation of sufficient thermal energy in the lattice will result in thermal vaporization of atomic material from the surface. The classic modeling of thermal evaporation is developed from a kinetic description that generates a couple of familiar laws: The velocity distribution is Maxwell–Boltzmann, and the angular distribution of the flux is isotropic, following the Knudsen cosine law. However, interpretation of the relative success or failure of the thermal description with respect to experimental data has always been a highly subjective, even controversial topic. Gibert *et al.* [34] produced a very interesting study of near-threshold sputtering of a Fe target irradiated with a N_2 laser beam ($\lambda = 337$ nm, $\tau_p = 10$ ns, $F = 50$–320 mJ/cm^2). They found (1) Maxwellian velocity distributions for both Fe$^+$ ions and Fe atoms, (2) a broad agreement between the translational and internal excitation energies of the monatomic plume constituents — indicating thermal equilibrium between these modes of energy storage, and (3) that temperatures corresponding to translational and internal excitation energies were consistent with melting and evaporation of Fe. The principal conclusion of Gibert *et al.* concerning the mechanism of laser sputtering of Fe was that pulsed laser sputtering of Fe is a thermal phenomenon.

The tacit assumption made in the conventional description of evaporation (and sublimation) is that the nascent atomic vapor flux leaves the

surface with the same energy distribution with which a uniform motionless vapor, in thermal equilibrium with the surface phase, would condense to that surface. In short, the vapor phase leaves the surface with a half-Maxwellian velocity distribution. In the literature, the region immediately adjacent to the irradiated surface is called the *Knudsen layer*. Within this region, interparticle collisions impart the trajectories and energy to the vapor particles recondensing on the surface. Thus, the Knudsen layer is characterized by a nonequilibrium gas kinetics description. The collisions between vapor particles leaving the surface eventually establish thermodynamic equilibrium in the gas and a finite extent to the Knudsen layer. The thickness of the Knudsen layer is generally recognized to be in the order of a few mean-free paths from the surface. Under conditions of large material flux from the surface, the mean-free path between collisions is small, resulting in a very thin Knudsen layer. In the case of a high-vacuum environment and low material fluxes, the vapor plume is largely collisionless.

Several studies have focused on the role of the Knudsen layer formation in laser vaporization, sputtering, and decomposition. Kelly and Dreyfus [49] showed that under the condition that the particle emission is driven by a thermal mechanism, the ejection velocities at the target surface are described by a half-range Maxwellian distribution. For as few as three collisions per particle, a Knudsen layer forms, which is confined within a few mean-free paths from the solid surface. Within this Knudsen layer, the density distribution function evolves to a full-range Maxwellian in a center of mass coordinate system. Moreover, Kelly and Dreyfus [50] showed that the Knudsen layer formation leads to forward peaking of the kinetic energy distributions of the ejected particles. Angular profiles following $\cos^4 \theta - \cos^{10} \theta$ functions were thus expected, in general agreement with experimental measurements. For evaporation yields exceeding, for instance, half of a monolayer per a 10-ns laser pulse, Kelly [47, 48] showed that the resulting gas-phase intractions cause the Knudsen layer to evolve into an unsteady, adiabatic expansion. An explicit solution for the speed of sound and the gas velocity was obtained, emphasizing the importance of the Mach number and the specific-heat ratio ($\lambda = C_p/C_v$) in the interpretation of experimental time-of-flight (TOF) measurements. Comparison of the gas dynamics model with numerical solutions of the flow equations and with direct simulations of the Boltzmann equation by Sibold and Urbassek [92] and Knight [57] showed reasonable agreement, despite the inherent assumption of local thermodynamic equilibrium (LTE). Finke *et al.* [30] and Finke and Simon [29] treated the steady-state formation of the Knudsen layer numerically by solving the Boltzmann equation using an integral approach. Their solution yielded temperature, mass density, and

velocity distributions in the Knudsen layer, as well as the decrease of pressure along the ejected vapor stream.

B. TIME-OF-FLIGHT MEASUREMENTS

Stritzker *et al.* [96] and Pospiesczyk *et al.* [79] used a quadrupole mass spectrometer (QMS) in a TOF arrangement to determine the kinetic energies of evaporated Si and GaAs targets by 20-ns long pulsed ruby laser irradiation. On the basis of these energy distributions, they extracted the temperature of the evaporated atoms by fitting Maxwellian distributions from gas kinetic theory. Furthermore, by assuming that this temperature represented the lattice temperature, they concluded that the process was thermal. It is tempting to conclude that the TOF measurements offer an appealing means of characterizing the thermal conditions of the ejected plume. At this point, it is worthy to recall the basic principles of such measurements.

The expection of a Boltzmann energy distribution in TOF measurements can obtain from formal gas dynamics. The number density of vapor particles having velocities between $\mathbf{u} = \langle u_x, u_y, u_z \rangle$ and $\mathbf{u} + d\mathbf{u} = \langle u_x + du_x, u_x + du_y, u_z + du_z \rangle$ liberated from the surface is

$$dn_s(\mathbf{u}) = dn_s(\mathbf{u})/u_x = n_s f(\mathbf{u}) \, du_x \, du_y \, du_z, \qquad (38)$$

where n_s is the total vapor number density at the surface and the Maxwellian velocity distribution function is given by

$$f(\mathbf{u}) = \left(\frac{m}{2\pi k_B T} \right)^{3/2} \exp\left[-\frac{m\left(u_x^2 + u_y^2 + u_z^2 \right)}{2 k_B T} \right]. \qquad (39)$$

When the surface flux temporal behavior is approximated by a delta function, the number density velocity distribution becomes spatially resolved as higher velocity particles move farther from the surface than lower velocity particles in a given period of time. If the surface flux is approximated by a point source, and the particle stream is collisionless, the following TOF approximations can be made

$$u_x = -x/t \qquad du_x = xt^{-2} \, dt,$$
$$u_y = y/t \qquad du_y = dy/t - yt^{-2} \, dt = dy/t + (y/x) \, du_x,$$
$$\qquad\qquad du_y = dy/t(|y/x| \ll 1),$$
$$u_z = z/t \qquad du_z = dz/t - zt^{-2} \, dt = dz/t + (z/x) \, du_x,$$
$$\qquad\qquad du_z = dz/t(|z/x| \ll 1),$$

where x, y, and z are spatial coordinates and t is the time of flight. Since the number density of particles sweeping by the small area of the particle detector is of interest, it may be assumed that $|y/x| \ll 1$, $|z/x| \ll 1$ and that $|u_y|$, $|u_z| \ll |u_x|$ at the detector. Consequently, it may be anticipated that the detector signal is

$$N_d(t) \, dt = \iint \left[n_s f(\mathbf{u}) \, x t^{-4} \, dt \right] dy \, dz, \tag{40}$$

which, when integrated over the surface area of the detector, A_d yields

$$N_d(t) \, dt = A_d n_s f(\mathbf{u}) \, x t^{-4} \, dt, \tag{41}$$

recalling that at the detector $u_x^2 \gg u_y^2$, u_z^2 and $u_x = x/t$,

$$N_d(t) = A_d n_s (m/2\pi k_B T)^{3/2} x t^{-4} \exp\left\{ -(m/2k_B T)(x/t)^2 \right\}$$

or

$$N_d(t) \sim \frac{1}{t^4} \exp\left[-\frac{m(x/t)^2}{2k_B T} \right]. \tag{42}$$

The measured density signal, $N_d(t)$, can be converted into the physically more meaningful flux distribution, as a function of the translational energy $P(E)$ using the following relation:

$$P(E) \, dE = u_x N_d(t) \, dt. \tag{43}$$

Recognizing that $(dE/dt) \sim t^{-3}$ and $u_x \sim t^{-1}$, we can express (43) as

$$P(E) \sim t^2 N(t). \tag{44}$$

The translational energy is related to the flight time as

$$E = (m/2)(x/t)^2. \tag{45}$$

Combining Eqs. (42), (44), and (45), the TOF signal inverted into energy space is expected to be Boltzmann:

$$P(E) \sim E \exp\left(-\frac{E}{k_B T} \right). \tag{46}$$

In the limit of a small surface vapor flux, the vapor expansion into vacuum is collisionless and the mean translational energy should be indicative of the surface phase temperature, $\bar{E} = 2k_B T$. The characteristics of the translation energy distribution in the ablation plume for a gold target have been explored [9] using the QMS TOF system described in [90]. In that study, the material removal rates were kept small (≤ 10 Å per pulse), and it was verified that the laser intensity was not sufficient to ignite plasma effects in the vapor plume. Figures 21a–d demonstrate the effect of laser
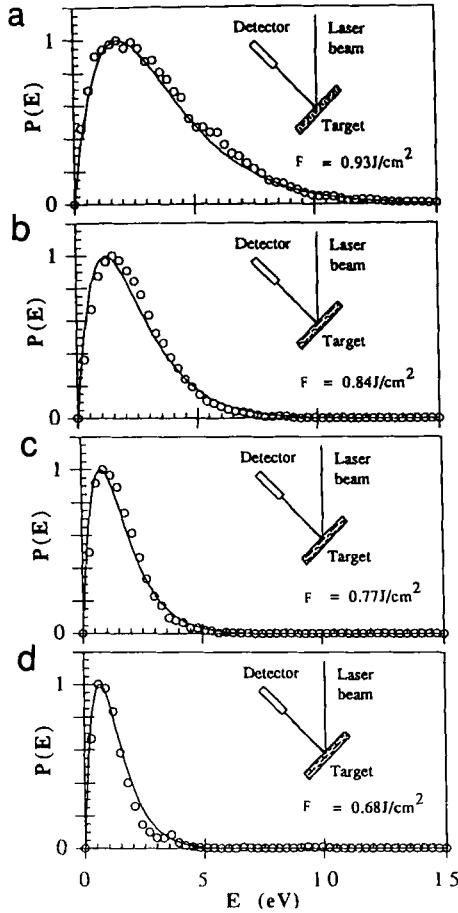
FIG. 21. Effect of laser fluence on the translational energy distribution of neutral Au atoms ($\theta_i = 45°$, $\theta_d = 0°$). The circles correspond to the inverted TOF signal; the solid line represents a Boltzmann distribution having the same mean energy as the inverted TOF signal ([9], reproduced with permission from AIP).

fluence on the kinetic energy distribution in the plume. The laser fluence has been varied from a near-threshold fluence (≈ 0.68 J/cm^2) to about 1.0 J/cm^2 over the course of this experiment. For this series of measurements, the detector was located normal to the surface and centered over the ablation area, and the laser beam was incident at 45° from the surface normal. Depicted in Fig. 21 are inverted TOF measurements in comparison with the theoretically predicted Boltzmann distribution. The first observation to be made from panels a–d (Fig. 21) is the apparent success

of the Boltzmann distribution in describing the energy distribution in the plume. The second finding is that the measured mean kinetic energies (up to several electronvolts) correspond to temperature far exceeding the thermal expectations (1 eV ~ 11,620 K).

The meaning of the "temperature" derived from the mean translational energy is further explored. It was shown before that when near surface collisions are rare, the density sensitive TOF signal should vary as

$$N_d(t) = \frac{1}{t^4} \exp\{-\Gamma^2 x^2/t^2\}, \tag{47}$$

where $\Gamma^2 = m/(2k_B T)$. However, with the development of a stream velocity $\bar{u}$, the flight distance relative to coordinates moving at $\bar{u}$ becomes $\bar{x} = x - \bar{u}t$, so the Eq. (47) becomes

$$N_d(t) = \frac{1}{t^4} \exp\{-\bar{\Gamma}^2(x - \bar{u}t)^2/t^2\}, \tag{48}$$

where $\bar{\Gamma}^2 = m/(2k_B \bar{T})$. Using Eq. (44), the temporal behavior of the density signal can be converted into a flux-sensitive energy distribution:

$$\tilde{P}(E) \sim E \exp\left\{-E/k_B\bar{T} + 2\bar{\Gamma}\bar{u}\left(E/k_B\bar{T}\right)^{1/2} - \bar{\Gamma}^2\bar{u}^2\right\}. \tag{49}$$

Kelly and Dreyfus [50] have argued that $\bar{u}$ is at least the sonic velocity at the outer edge of the Knudsen layer. If this is assumed, then for a monatomic perfect gas, $\bar{u} = (5/6)^{1/2}\bar{\Gamma}$, and Eq. (49) becomes

$$\tilde{P}(E) \sim E \exp\left\{-E/k_B\bar{T} + 2\left(5E/6k_B\bar{T}\right)^{1/2} - 5/6\right\}. \tag{50}$$

The mean kinetic energy of the above distribution is $\bar{E} = 3.67k_B\bar{T}$. It is noted that the temperature in Eqs. (49)–(50) implicitly refers to the vapor temperature rather than the surface temperature. Nevertheless, Fig. 22 shows that the Boltzmann distribution fits better the experimental results than the "stream-velocity-corrected" distribution. The implication is that an order of 10 or 20 collisions per particle that is obtained by a simple estimate for the material removal rates considered is not sufficient to impart a significant stream velocity.

The energy coupling between the incident laser beam and the target surface evolves with surface topography as the ablation of the surface proceeds. To investigate this affect, the plume energy has been measured while an initially "virgin" surface is repeatedly pulsed with laser light. The number of counts per pulse registered by the detector was analyzed as the total number of accumulated pulses grew (Fig. 23a). Figure 23b shows the development of plume energy distributions (fitted by Boltzmann distribu-
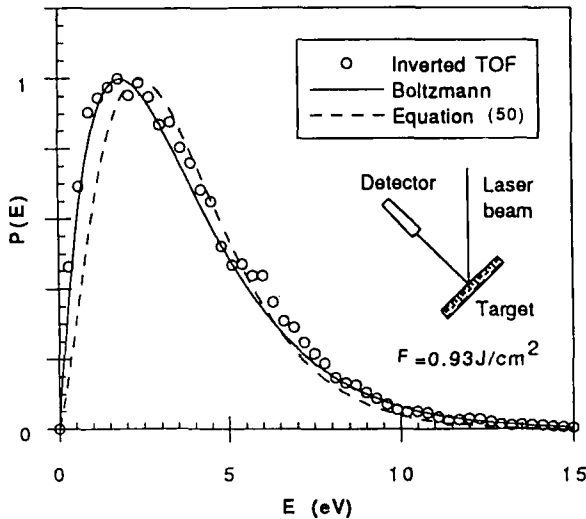
FIG. 22. A direct comparison between experiment, a Boltzmann energy distribution, and a Knudsen layer perturbed energy distribution, as suggested by Kelly and Dreyfus [50] ([9], reproduced with permission from AIP).

tions) as the number of pulses increases. The energy distribution demonstrate increasing mean energy, 3.9–5.7 eV, with increasing accumulation of laser pulses. It is evident that energy coupling eventually reaches a steady-state condition—apparently at 300 laser pulses for the case illustrated here. Kelly *et al.* [52] observed that the ablation rate decrease with increasing surface roughness. Krebs and Bremert [62] found that as surface topography developed, the ablation rate decreased by 30–40% before reaching its steady-state value.

C. Considering Thermal and Electronic Effects

Until recently, the thermal nature of pulsed laser sputtering from metals has been questioned by relatively few researchers. The wisdom of a thermal description is supported by the conventional picture of how metals absorb radiative energy. Photons are thought to interact almost exclusively with the conduction band electrons of metals, which often are modeled as a free electron gas irrespective of whether the phase is liquid or solid. In contrast to insulators and semiconductors, incident photons excite conduction band electrons in metal without perceptible lattice relaxation, and there is no energetic electron–hole recombination event in the absence of
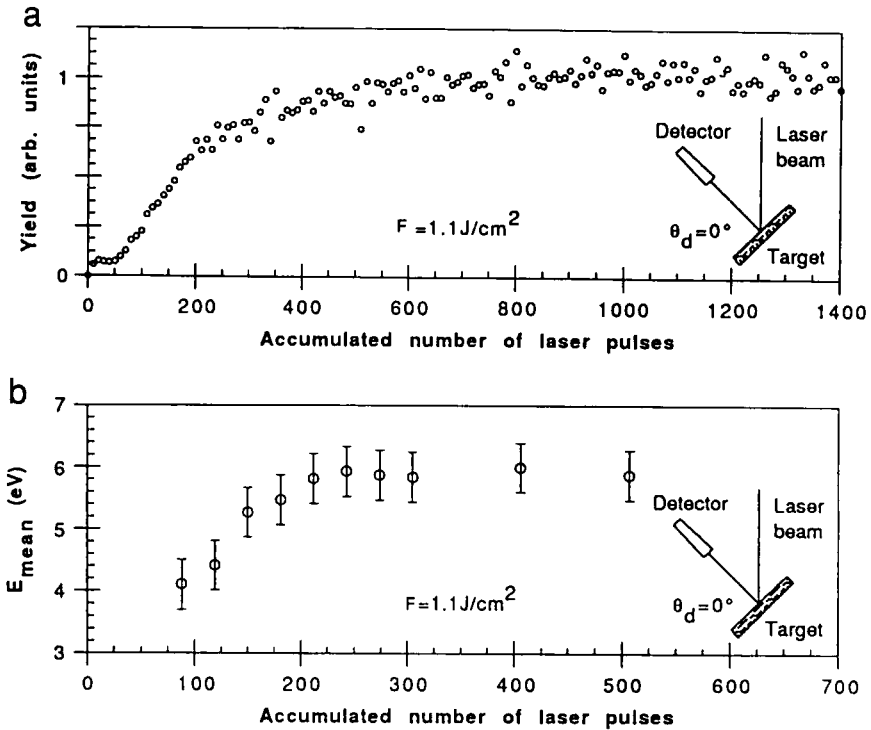
FIG. 23. (a) Sputtering yield and (b) mean translational energy of neutral gold atoms vs. accumulated number of laser pulses on an initially virgin surface ([9], reproduced with permission from AIP).

a bandgap. Consequently, there is no conventional mechanism to localized electronic energy in metals. Instead, energetic electrons relax through scattering events with phonons, thereby transferring energy to the lattice. On the time scale of a nanosecond-range laser pulse, the cascade of energy is continuous with thermal heating of the lattice. Electron thermalization in gold occurs in the time scale of ~500 fs (femtoseconds) [27] and electron–phonon energy relaxation occurs on the time scale of ~1 ps. Energy transport (conduction) in metals is accomplished principally by electron–electron scattering and lattice heating, by electron–phonon scattering. Because of momentum conservation, energetic electrons are prohibited from localized decay during a scattering event. As heat stored in the condensed phase rises, the high-energy tail of the phonon distribution provides sufficient energy for surface atoms to overcome their binding

energy and escape to the vapor phase. The energy and momentum require-
ments for desorption are met by the lattice.

Recent experimental results, however, have challenged the conventional
view that nanosecond pulsed laser vaporization of metal can always be
absorbed to thermal mechanisms [40, 53, 65, 90]. These studies have
explored nonthermal desorption from metal at low laser fluences from the
solid phase. The apparent consensus is that the creation and local decay of
a surface plasmon (a collective excitation of electrons) is responsible for
discharging energetic atoms from metals. The principal issues concerning
the role of plasmons in desorption are (1) the conditions required to excite
plasmons and (2) how the plasmon energy is converted into the transla-
tional energy a single atom. Most attention has been given to the first
question. The probability of exciting a surface plasmon with an incident
photon is reduced by the typical mismatch in phase velocities of a plasmon
and a photon having the same energy. Consequently, specialized geome-
tries have been used to investigate the role of surface plasmons in
desorption. To enhance coupling with surface plasmons, prisms have been
used to slow the phase velocity of photons, whereas geometries leading to
total internal reflection orient the wavevector parallel to the surface. Kim
and Helvajian [53] and Lee *et al.* [65] have both reported energetic
desorption from thin metal films using this geometry. Surface plasmons
can also be excited on small metallic spheres, as realized classically by Mie
theory. Coupling is strongest when the sphere is small compared to the
photon wavelength. Hoheisel *et al.* [40] have observed resonantly enhanced
desorption rates from metallic clusters (Na, K) of radii roughly 10% of the
photon wavelength. Observations of energetic desorption from fairly
generic conditions have led some researchers to relax the usual anticipated
conditions for surface plasmon excitation [53]. It has been experimentally
demonstrated that the conversion of photon energy to surface plasmon
energy can be facilitated by surface roughness. The purest experimental
demonstration of this is found using diffraction gratings. The reciprocal
space vector of the grating can augment the plasmon wavevector to match
the incident photon wavevector (parallel to the surface). In this manner,
both energy and momentum can be conserved. A conceptually straightfor-
ward extension of this can be made to surfaces of arbitrary roughness. The
surface roughness provides a characteristic momentum spectrum that can
selectively furnish the momentum requirements of the photon-to-surface
plasmon energy conversion. A detailed account of coupling between sur-
face plasmons and phonons is given in a review article by Ritchie [81].

The second question, of how the plasmon energy is coupled to desorp-
tion, is more difficult to resolve. Some theoretical consideration has been
given to the problem [82], however, the mechanism for localizing the

plasmon energy to a single atom remains unclear. Even the most energetic plasmons carry very little momentum—necessitating a three-body collision process between the desorbing atom, plasmon, and the lattice (which provides the required momentum) to satisfy the conservation laws. Recent appeals to plasmon induced desorption have emphasized various and sometimes contradictory features of the process. For example, the energy of desorption is insensitive to fluence [40, 65, 90]; the desorption energy is equal to the plasmon energy [90]; the desorption yield has a linear dependent on fluence [40, 65]; the desorption yield has a superlinear dependence on fluence [82, 90]; and desorption is resonant at photon energies near the plasmon energy [40, 90].

An experiment has been constructed [10] that extends previous notions of the nature of pulsed laser sputtering from metals. In this experiment, laser fluences are sufficiently high to study vaporization from the liquid phase. In desorption processes from the solid state it is not always clear how to specify cohesive energy, bonding state, and electronic structure of surface atoms. The high atomic mobility of liquid metals, however, suppresses any distinction between surface states and, for metals, the first-order electronic structure remains the same as for the solid phase. Another benefit of surface melting is that surface structures with dimensions smaller than the laser wavelength have very short damping periods while in the liquid phase. Consequently, small structures most amenable to photon coupling with surface plasmons are removed rapidly by the liquid surface capillary action. An additional degree of freedom introduced in the study by Bennett *et al.* [10] allows the total energy delivered to the target to be partitioned between steady-state electron-beam heating of the back surface and pulsed laser heating of the front surface. This configuration permits investigation of the effect of variable electronic energy density (provided by the laser) for the same thermal conditions, illuminating what effect this has on the mean translational energy of vaporization.

The target steady-state temperature is controlled by electron-beam (e-beam) heating. A resistively heated tungsten filament, held at ground potential behind the target, thermally emits electrons that are accelerated into the target, which is held at +100 V. As little as 2 W of e-beam heating is sufficient to raise the target temperature 800 K above the ambient temperature. Pulsed laser melt annealing is performed at high temperature and relatively low laser fluences to minimize the hydrodynamic formation of surface topography during annealing. After melt annealing, the mean variation in local surface normals is about ±3° (measured by atomic force microscopy (AFM)).

Figure 24 shows yields and translational energies of Au° for initial target temperatures of 375 and 1100 K. The two ranges of investigated fluences
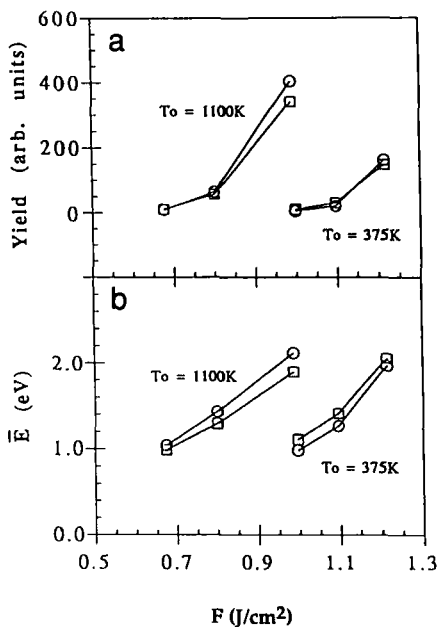
FIG. 24. Au° yield and mean translational energies in the first 10 (○) and the second 10 (□) laser pulses on the annealed target surface. Data for two initial target temperatures (To) are shown; (a) shows yields and (b) depicts translational energies [10].

are offset to keep the peak thermal conditions comparable for the different initial temperatures. The upper bound on the fluence range investigated is maintained below the onset of gas-phase plasma formation. For both temperature cases the mean translational energy correlates positively with laser fluence. There is no evidence of a single preferred desorption energy as has been suggested in connection with the local decay of a surface plasmon. In addition, the yield demonstrates a superlinear dependence on laser fluence. This suggests that the desorption process is not a single-photon process. Researchers investigating plasmon-induced desorption have been divided on this point. The scenario in which a plasmon decay couples with an antibonding electronic transition favors a linear dependence between yield and fluence [40]. However, it has also been suggested that desorption can be mediated by a thermal process, such that the local decay of a surface plasmon served only to enhance the desorption energy [82, 90]. In this case, yields should be superlinear with respect to laser fluence. However, there is only a finite probability for thermally ejected atoms to be recipients of the plasmon energy—leading to the

prediction of a bimodal energy distribution. No condition investigated in the present work produced a bimodal energy distribution.

The mean translational energy of gold atoms leaving the surface can be compared with anticipated thermal energies based on numerically calculated surface temperatures. The numerical calculation uses the enthalpy method described in Section I, with a change in the surface boundary condition. The surface boundary condition is now prescribed by a kinetic relation between the surface temperature and vapor flux [see Eq. (51)]. There are several salient features to this comparison, as shown in Fig. 25. The first is that actual mean translational energies are at least a factor of 2–3 higher than the thermal expectation. In addition, the slope in energy with respect to temperature is approximately $15k_B$ instead of $2k_B$ as would be predicted for a thermal process.

Certainly, the most perplexing question is how the desorption process produces such high kinetic energy. Is the electronic energy density in the metal more or less important than the thermal "lattice" energy with respect to the energetic desorption process? To address this question, the energy delivered to the target surface has been partitioned between steady-state electron-beam heating of the back surface and pulsed laser heating of the front surface. The laser heated surface achieves the same peak temperature (approximately 2760 K) for all experimental conditions shown in Fig. 26. However, the laser contribution to the peak surface energy increases from 60 to 87%, progressing from left to right in the figure. Figure 26 shows no appreciable change in yield of Au° or mean translation energy. The constant yield is strong evidence that this aspect of
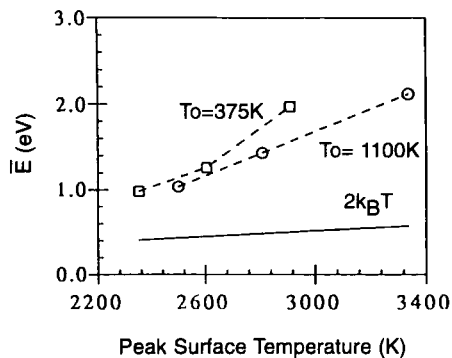

FIG. 25. Measured and thermally anticipated $(2k_B T)$ translational energies as a function of calculated peak surface temperature. The data pertain to the first 10 laser pulses on the annealed target surface [10].
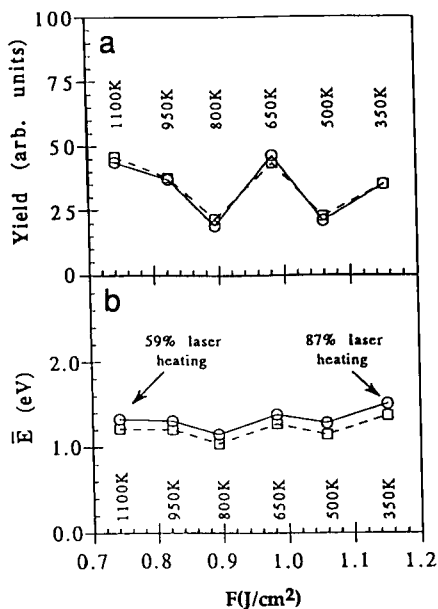
Fig. 26. Au° yield (a) and mean translational energies (b) in the first 10 (○) and the second 10 (□) laser pulses on the annealed target surface. The peak surface temperature (~ 2680 K) is approximately the same for all initial target temperature–laser fluence combinations [10].

the desorption process is governed by thermal conditions at the target surface. The fact that the mean translational energy is also nearly constant is a very interesting result indicating that desorption energy is most sensitive to the peak surface temperature and does not appear to be a strong function of the electronic energy density alone.

A remarkable characteristic of the measured translational energy distributions is the closeness to Boltzmann form. Figure 27 shows two energy distributions for the initial target temperature of 375 K. The shape of the energy distribution is surprising only because it is reminiscent of a thermal process—despite the fact that energies are much too high to reconcile with the classic thermal model. However, the shape of the energy distribution does suggest that the source of desorption energy is not connected with a quantized value, such as the plasmon energy. If a decaying surface plasmon somehow transfers its energy to desorption, one might expect the energy distribution to be either a delta function at the plasmon energy or perhaps a Boltzmann function offset by the plasmon energy. Neither of these possibilities is suggested by the observed energy distribution.
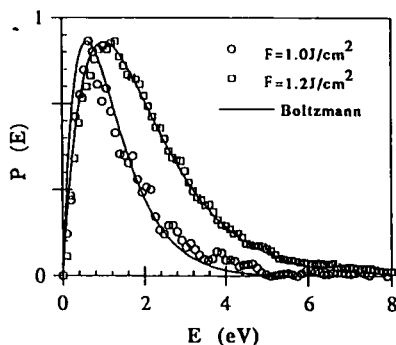
FIG. 27. Comparison of measured energy distributions with Boltzmann fits for the first 10 laser pulses on the annealed surface. The initial target temperature for both cases is 375 K [10].

The fact that our irradiation geometry is not conducive to plasmon excitation (at least by design), the fact that yields are superlinear with laser fluence, and the fact that Au translational energy distributions are neither bimodal nor peaked about a quantized value all suggest that the plasmon-induced desorption picture is deficient, at least with respect to terms suggested by earlier researchers. However, it is also clearly premature to rule out involvement of surface plasmons, particularly since the superthermal translational energy of desorption makes transparent the inadequacy of the conventional description. The theoretical basis for surface plasmon-induced desorption is perhaps too underdeveloped to formulate solid expectations for this process.

III. Computational Modeling of Pulsed Laser Vaporization

A. BACKGROUND

Various theoretical models have been proposed to describe material removal from a solid heated by laser irradiation. The thermal models of Afanas'ev and Krokhin [3], Anisimov [4], and Olstad and Olander [74] represent early theoretical contributions to this problem. Chan and Mazumder [16] developed a one-dimensional steady-state model describing the damage caused by vaporization and liquid expulsion due to laser−material interaction. Much of the work in those studies was driven by laser applications such as cutting and drilling, and was thus focused primarily on the target morphology modification, with no particular inter-

est in the detailed description of the properties and dynamics of the evaporated and ablated species. Moreover, these models dealt with continuous-wave (CW) laser sources, or relatively long (millisecond-range) time scales.

During the first stage of interaction between the laser pulse and the solid material, part of the laser energy is reflected at the surface and part of the energy is absorbed within a short penetration depth in the material. The energy absorbed is subsequently transferred by heat conduction deeper into the interior of the target. At a later stage, if the amount of laser energy is large enough (depending· on the pulse length, intensity profile, wavelength, the thermal and radiative properties of the target material), melting occurs and vaporization follows. The vapor generated can be ionized, creating a high-density plasma that further absorbs the incident laser light. The physical picture of laser energy interaction with evaporating materials at high fluence ($F > 1$ GW/cm^2) then becomes quite complicated. Of interest are the descriptions of the vaporization and ionization processes, the associated fluid motions and gas dynamics phenomena (including the vapor–plasma expansion and possible shock wave formations against the ambient environment pressure), and the intense electromagnetic fields generated [77].

Phipps *et al.* [78] developed a simple model to predict the ablation pressure and the impulse exerted on laser irradiated targets for laser intensities exceeding the plasma formation threshold. The model was shown by Phipps and Dreyfus [77] to follow the experimental trends for the mass loss rate and the ablation depth within a factor of 2. In their computational studies, Aden *et al.* [1, 2] dealt with the laser-induced expansion of metal vapor against a background pressure. Using a compressible gas dynamics numerical model, they were able to capture the development of shock discontinuities in the vapor phase, in agreement with experimental observations. Vertes *et al.* [102, 103] developed a one-component, one-dimensional model to describe the expansion of laser-generated plasmas. The model incorporated the conservation equations for mass, momentum, and energy. Singh and Narayan [93] proposed a theoretical model for simulation of laser–plasma–solid interactions, assuming that the plasma formed initially undergoes a three-dimensional isothermal expansion followed by an adiabatic expansion. This model yielded athermal, non-Maxwellian velocity distributions of the atomic and molecular species, as well as thickness and compositional variations of the deposited material as functions of the target–substrate distance and the irradiated spot size.

Further research is needed to enable direct prediction of pulsed laser interactions with materials. In particular, it is necessary to address in detail

the heat transfer and fluid flow phenomena that occur in the associated phase-change transformations from the solid to the liquid, and from the liquid to the vapor phases.

B. Modeling Description—Transparent Vapor Assumption

It is sought to construct a numerical model for the computation of the heat transfer in the substrate, including the melting transformation and the following vaporization. It is assumed that a metal target is subjected to pulsed laser radiation and that the ejected vapor plume expands against an inert gas of reduced pressure. Figure 28a depicts a laser pulse incident on a bulk substrate and shows the generated melt region and the ejected vapor plume. The laser beam spot shape is assumed to be circular, of radius $r_{las} = 1$ mm and of uniform intensity distribution profile. In the thermal description of the phase transition from liquid to the vapor, it is necessary to cross the vaporization dome. This is accomplished by introducing a discontinuity layer just above the liquid surface. The physical origin and significance of the discontinuity layer are discussed next.

In the classic kinetic model of evaporation, the vapor particles escaping from a hot liquid surface possess a half-Maxwellian distribution, corresponding to the liquid surface temperature. The velocity vectors of these particles point away from the liquid surface. The anistropic velocity distribution is transformed into an isotropic one by collisions among the vapor particles within a few mean-free paths (typically of the order of few micrometers) from the surface in a discontinuity region known as the *Knudsen layer* (Fig. 28a). Some of the particles experience large-angle collisions and are scattered back to the surface. Beyond the discontinuity layer, the vapor reaches a new internal equilibrium at a temperature different from the surface temperature (usually lower than the liquid surface temperature). Appropriate boundary conditions are needed for the vapor phase on the vapor side of this discontinuity layer (Fig. 28b). In order to derive these boundary conditions, the conservation equations for mass, momentum, and energy are applied across the discontinuity layer. There are two models for describing laser-induced vaporization: the solid/vapor-phase transition and the liquid/vapor-phase transition. If the intensity of the incident radiation exceeds a certain threshold, then the temperature of the target material within the penetration depth ($\sim 10^{-8}$ m) exceeds the normal boiling temperature of the metal and is certainly higher than the melting temperature. Thus, the liquid/vapor-phase transition model is used in this study. Also, the difference between the two modes is fundamental. Only within the framework of the liquid–vapor transition is it possible to consider the intensity region
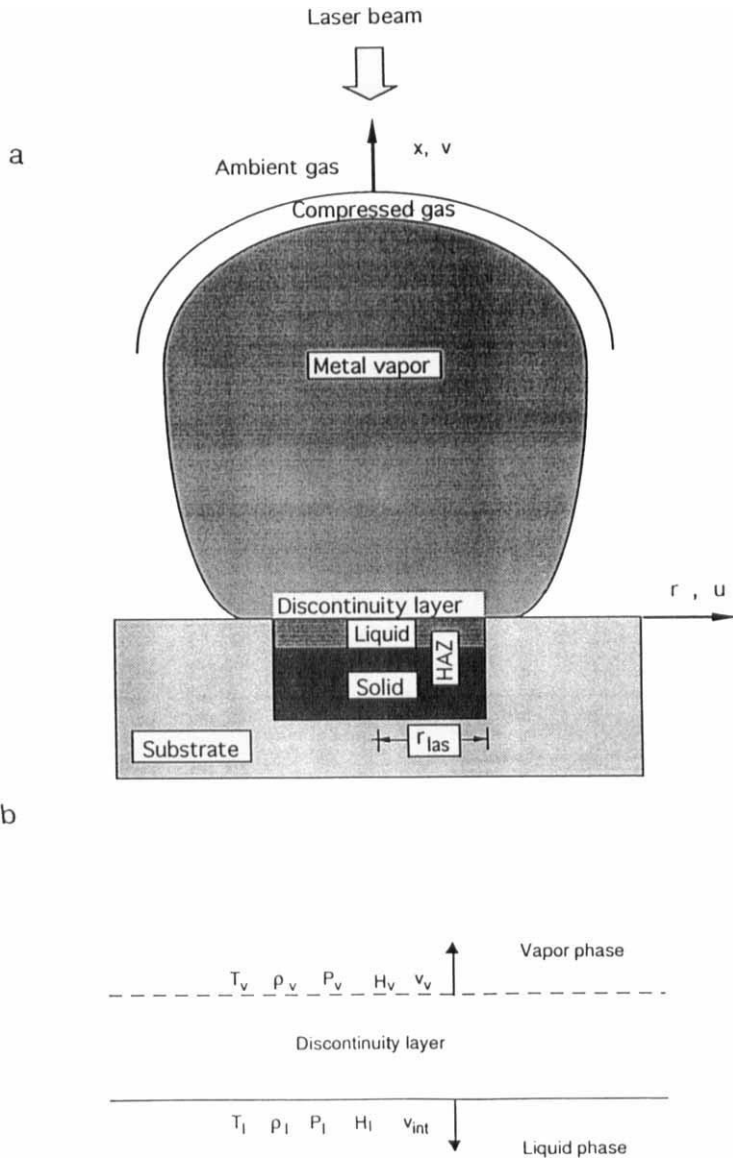
FIG. 28. (a) Diagram of laser-induced vaporization from a metal surface showing the heat-affected zone (HAZ), the various phases, and the coordinates of the computational domain; (b) diagram showing the variables across the discontinuity layer between the evaporating liquid surface and the vapor phase ([39], reproduced with permission of AIP).

corresponding to a metal surface temperature approaching the critical temperature [7]. It is also assumed that the vaporization mechanism is "surface vaporization," that is, that no bubbles are formed prior to or during the liquid evaporation process. These two mechanisms are substantially different. For media that are free from impurities, entrapped gases and structural microdefects such as microcracks and pores, and that absorb radiation to a depth of 10^{-6} m, it is estimated that volumetric radiation can be an effective means of material removal in comparison with surface vaporization only at temperatures close to $0.3L_v/k_B$ [84]. For common metals, particularly Al, Au, and Cu, which are considered in this work, this value exceeds 10^4 K. Another reason for the assumption of "surface evaporation" is that the surface tension coefficients of liquid metals are large during the lifetime of the liquid–metal layer [7].

The heat transfer in the substrate is calculated by applying the enthalpy scheme presented in Section I.B. As long as the vapor is considered transparent to the incident laser radiation, nonemitting, and non-heat-conducting, the heat transfer in the substrate is not affected by the vapor plume. Hence, considering that the beam radius is again much larger than the thermal penetration depth, it is inferred that the heat transfer in the substrate is one-dimensional. Assuming that the liquid behaves like a dense gas, the rate of evaporation from the liquid surface, j_{ev}, can be derived using kinetic theory [15, 97] as

$$j_{ev} = n_l \left(\frac{k_B T_l}{2\pi m_a} \right)^{1/2} \exp\left(-\frac{L_v}{k_B T_l} \right) - \theta_s n_v \left(\frac{k_B T_v}{2\pi m_a} \right)^{1/2}, \qquad (51)$$

where the first term in the right side represents the evaporation rate from the liquid surface at temperature T_l. The second term represents a damping of this evaporation rate due to the return of vapor molecules to the liquid surface. According to the analyses by Anisimov [4], Batanov et al. [7] and von Allmen [104], the upper limit for the entrapment of vapor molecules returning to the liquid surface is below 20%. The parameter θ_s, the "effective sticking coefficient," represents the probability of a vapor atom returning to the liquid surface from equilibrium conditions at the edge of the discontinuity layer manages to penetrate this layer to finally be adsorbed on the liquid surface. This parameter is chosen so as to yield a recondensation to evaporation rate in the range from 15 to 20%.

The conservation equations of mass, momentum, and energy applied to the discontinuity layer are as follows:

Mass conservation:

$$\rho_v(-v_v - v_{int}) = \rho_l(v_l - v_{int}). \qquad (52)$$

Momentum conservation:

$$P_v - P_1 = \rho_v(-v_v - v_{int})(v_1 + v_v). \tag{53}$$

Energy conservation:

$$H_1 + L_v = H_v + \tfrac{1}{2}(v_v^2 - v_1^2). \tag{54}$$

An equation of state for the liquid is also needed for the calculations. A possible choice is the van der Waals equation of state. This equation is representative of a class of equations of state that are reasonably accurate, embodying the main features of most condensable gases [8]. Unfortunately, however, the van der Waals constants are not available from experiments to represent the liquid metal behavior from melting to the critical state. In this study, it is assumed that (1) the temperature rise and phase transitions take place under conditions of local quasi-equilibrium, allowing the use of classical thermodynamics relations; and (2) the liquid expansion takes place along the liquidus line.

The first assumption simplifies the physical description of the problem. The choice of the liquidus line as the thermodynamic path for expansion is somewhat arbitrary, although it appears to be reasonable [8]. Thus, the liquid pressure, according to experimental values [41], can be expressed as

$$\log P_1 = \frac{a_1}{T_1} + a_2 \log T_1 + a_3. \tag{55}$$

It is also found experimentally that the temperature dependence of the density for liquid metals is linear and is accurately represented by the equation

$$\rho_1 = \rho_m - \Lambda(T_1 - T_m). \tag{56}$$

Since the ejected vapor is modeled as an ideal gas, the enthalpy of the vapor phase, H_v, is a function of the vapor temperature only, $H_v = H_v(T_v)$. The liquid surface temperature, T_1, and the energy content associated with the liquid, H_1, are directly calculated from the heat conduction in the substrate. One more assumption needed to close this system of equations is that the regression velocity of the liquid phase is very small, $v_1 \sim 0$, when compared with the regression velocity of the vapor–liquid interface and the forward expansion velocity of the vapor. Because the liquid layer is thin, and since a one-dimensional model is applied for the heat transfer in the substrate, this assumption is reasonable.

The vaporized material ejected from the liquid surface is modeled as a compressible, inviscid ideal gas. For the millimeter size of the laser spot diameter, which is the characteristic dimension in this problem, the continuum approach is expected to be valid for an ambient pressure $P_\infty = 10^{-4}$

atm. At lower pressures, the continuum framework is no longer valid [11] and a calculation approach suited for rarefied media, such as the direct particle collision simulation, is required. The dynamic state of the metal vapor phase is described by the compressible and nondissipative Euler conservation equations for mass, momentum and energy:

Mass conservation:

$$\frac{\partial \rho}{\partial t} + \text{div}(\rho \mathbf{V}) = 0. \tag{57}$$

Momentum conservation:

$$\rho \frac{\partial \mathbf{V}}{\partial t} + \rho(\mathbf{V} \cdot \text{grad})\mathbf{V} = -\text{grad}\, P. \tag{58}$$

Energy conservation:

$$\rho \frac{\partial e}{\partial t} + \rho(\text{grad})\mathbf{V} = -P \,\text{div}\,\mathbf{V}. \tag{59}$$

Two more equations define the total energy per unit mass, E_t

$$E_t = e + \tfrac{1}{2}(u^2 + v^2) \tag{60}$$

and the equation of state for an ideal gas

$$P = (\gamma - 1)\rho e, \tag{61}$$

where γ is the ratio of the specific heats, $\gamma = C_p/C_v$. Equations (56)–(61) are solved for ρ, u, v, E_t, P, and e in an axisymmetric (cylindrical) calculation domain using the MUSCL Eulerian compressible gas dynamics scheme [21]. It is assumed that vaporization takes place on a circular area, with no dependence on the azimuthal coordinate direction.

Computations were done for aluminum, gold, and copper. Figure 29 shows the temperature–time history of the surface of a gold metal substrate for different values of the laser fluence. Initially, the surface temperature increases rapidly during the laser pulse duration (20 ns). It then decreases rapidly, back to room temperature. The profiles show a "flat" region at $T = T_m$ (1338 K) during which the surface temperature is equal to the melting temperature for solidification and beyond which no more liquid exists on the substrate. As shown in the first section of this chapter, the heat transfer in the target material and the melting process are governed by heat diffusion. Thus, Figs. 30a, b show that the maximum liquid surface temperature as well as the melting depth vary linearly with the laser pulse fluence. Considering this trend, and keeping in mind that the evaporation rate increases exponentially with temperature, as Eq. (51)
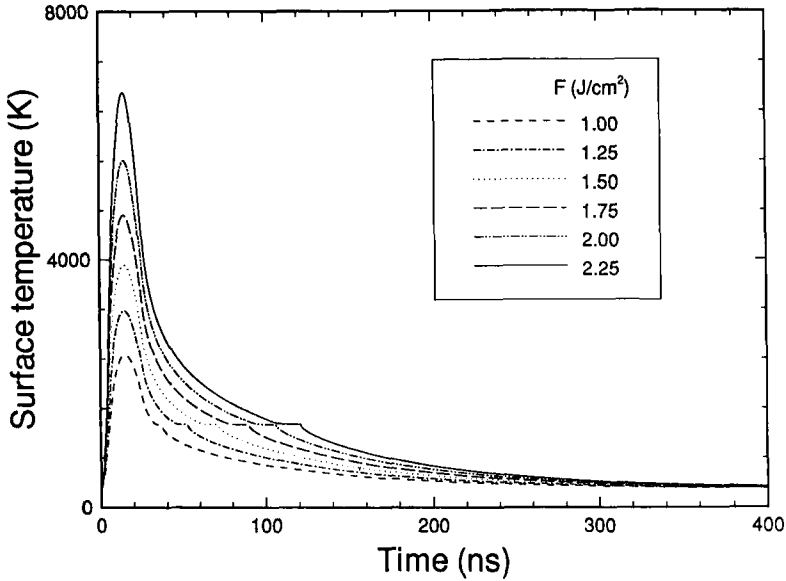
FIG. 29. Time histories of the surface temperature (ar $x \sim 0$) of a gold substrate subjected to excimer laser pulses of 26-ns duration and of different fluences. The ambient pressure is $P_\infty = 1$ atm, and the laser spot radius is $r_{las} = 0.5$ mm ([39], reproduced with permission of AIP).

shows, it is expected that the ablation depth increases exponentially with fluence as depicted in Fig. 30c. The dense liquid–solid substrate is subject to recoil forces exerted by the evaporating material. The total recoil momentum experienced by the irradiated body is

$$M_r = \iint P_{\text{recoil}} \, dA \, dt, \qquad (62)$$

where

$$P_{\text{recoil}} = P_v + P_{\text{ev}} - P_\infty . \qquad (63)$$

The term P_{ev}, defined as $\dot{m}_{\text{ev}} v_v / \pi r_{las}^2$, is due to the momentum change at the liquid–vapor interface. Figure 30c presents the recoil momentum, divided by the total energy E_0 carried by the laser radiation pulse, as a function of the laser fluence. Figures 31a–c shows normalized pressure contours in the vapor phase for a laser fluence $F = 1.75$ J/cm^2 incident on a bulk gold surface. The background pressure is set at $P_\infty = 10^{-3}$ atm, and the laser spot radius on the sample surface, $r_{las} = 0.5$ mm. The shock front, pushed by the high vapor pressure (hundreds of atmospheres)
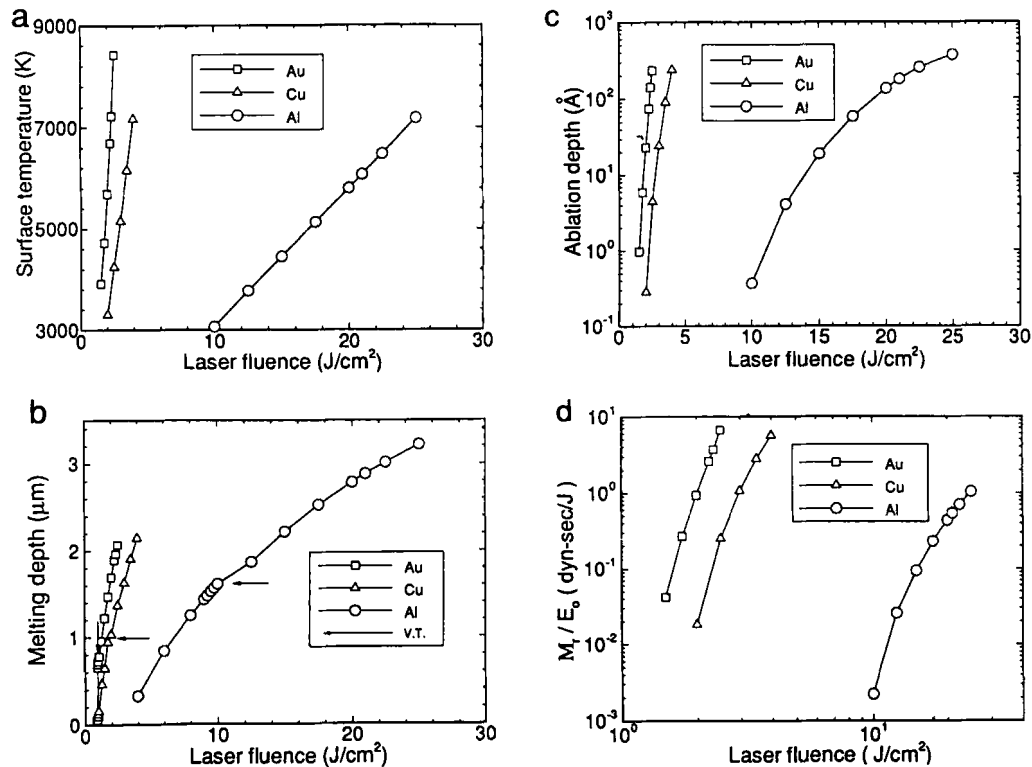
FIG. 30. (a) Maximum liquid surface temperature; (b) melting depth; (c) ablation depth; (d) dependence of vapor recoil momentum on laser fluence for Au, Cu and Al substrates subjected to excimer laser pulses of 26-ns duration and of different fluences. The arrows in panel b mark the vaporization thresholds (VTs). The ambient pressure is $P_\infty = 1$ atm, and the laser spot radius is $r_{las} = 0.5$ mm ([39], reproduced with permission of AIP).

FIG. 31. (a–c) Normalized pressure contours and (d–f) velocity vectors in the computational domain and for an Au substrate subjected to excimer laser pulses of 26-ns duration and of fluence $F = 1.75$ J/cm^2 at (a–d) $t = 1$ μs, (b–e) $t = 5$ μs, and (c–f) $t = 10$ μs. The ambient pressure is $P_\infty = 10^{-3}$ atm, and the laser spot radius is $r_{las} = 0.5$ mm ([39], reproduced with permission of AIP). The coordinate z is here normal to the substrate.

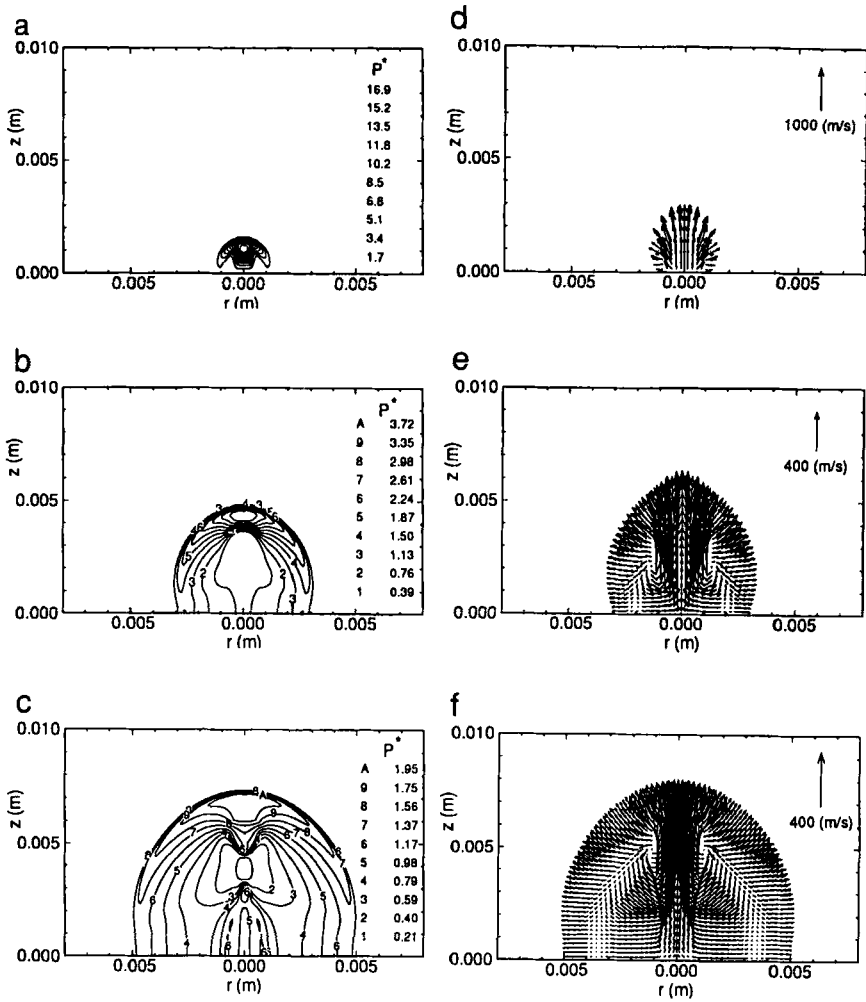produced during the laser pulse duration, propagates with an average speed of about 700 m/s into the ambient medium. For reference, it is noted that the sound speed for the ambient pressure and temperature is about 330 m/s. Figures 31d–f shows the corresponding velocity plots; they depict a situation similar in nature to the sudden explosion of the metallic target. The vaporized material is pushed upward and laterally simultaneously. As the vapor leaves the surface at high speed, it induces a recirculating zone of entrained fluid around it. Figures 32a–d show the normalized density ($\rho^* = \rho/\rho_\infty$), the normalized temperature ($T_v^* = T_v/T_\infty$), the vapor speed, and the local Mach number contours at a time $t = 5$ μs. It can be seen that most of the high-kinetic-energy material is concentrated in a jet-like core region moving at supersonic speeds normal to the surface. The outer region is an essentially motionless, isothermal, low-temperature zone.

The evaporating particles and the ambient gas have been assumed to be transparent to the incoming laser light. The validity of this assumption depends on the local plasma density. The plasma density determines the laser light-absorption coefficient. The mechanisms for absorption include inverse Bremsstrahlung and photoionization [116]. Computations of these effects on the plasma ignition and the laser energy coupling to the target were performed by Rosen *et al.* [83] and Duzy *et al.* [23] for microsecond-length UV laser pulses on aluminum. The degree of ionization can be estimated by invoking the Saha equation [18]

$$\frac{n_i^2}{n_n} \approx 2.4 \times 10^{21} T^{3/2} \exp(-U_i/k_B T), \tag{64}$$

where n_n and n_i represent the number of neutral and ionized particles per unit volume, respectively. For gold, the neutral particle density n_n is $O(10^{26})$, whereas the temperature of the evaporating particles is $O(10^3)$ during the vaporization period. The ionization potential, U_i, for gold is 9.22 eV. Hence, the corresponding n_i is $O(10^{21})$ and the estimated absorption coefficient is much smaller than $O(10^{-8})$ (m^{-1}). Thus, the assumption of an optically thin vapor phase is reasonable, at least with respect to the particular absorption mechanism in a gold vapor plume and for the range of fluences examined. For a thorough treatment, the densities of the neutral, excited, and ionic species must be calculated using rate equations for the radiative transitions and considering the electronic structure of the target materials. The absorption coefficient can then be derived and the laser energy transfer to the vapor plume as well as the radiation loss by thermal emission calculated by solving the radiative transfer equation. This is a brief outline of the computational procedure that is being implemented by Ho *et al.* [38].

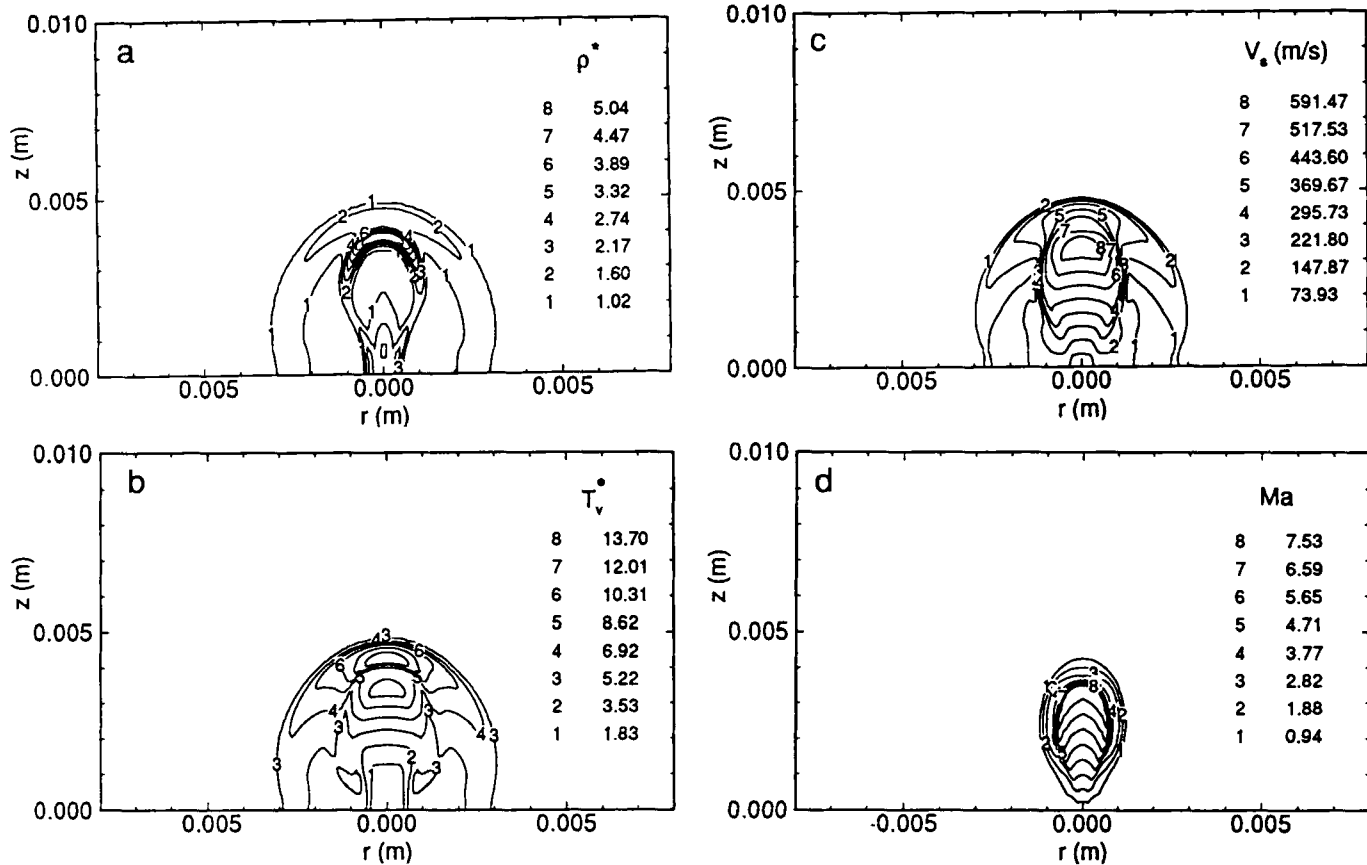FIG. 32. Contour plots for an Au substrate subjected to excimer laser pulses of 26-ns duration and of fluence $F = 1.75$ J/cm^2 at $t = 5$ μs: (a) normalized density; (b) normalized temperature; (c) vapor speed; (d) Mach number. The ambient pressure is $P_\infty = 10^{-3}$ atm, and the laser spot radius is $r_{las} = 0.5$ mm [39], reproduced with permission of AIP. The coordinate z is here normal to the substrate.

To compare with the computational results and characterize the laser-ablated plume, one would need to identify the various species (neutrals, ions, electrons, clusters, etc.) and measure their concentration and rates of generation and consumption, as well as their velocity and energy distributions. In addition, information about chemical reaction kinetics, as well as cross sections for a variety of processes in the laser-generated plasma, would be required. Comprehensive reviews of experimental studies of pulsed laser-induced ablative processes have been presented in Miller [69] and Chrisey and Hubler [20a]. Kinetic energies of the ejected particles can be measured using TOF [118, 119]. Laser-induced fluorescence (LIF) is another very useful diagnostic for laser ablation plasmas, providing number densities, kinetic energies, rotational temperatures and vibrational temperatures [72, 73]. Fast photography and other imagining techniques provide useful information for understanding the complex flow phenomena in pulsed laser ablation. The results of high-speed framing photography [88a], streak photography [26], and intensified charge-coupled device array (ICCD) photography of plume emission [32] as well as techniques using slower cameras and pulsed lasers for delayed imaging in Schlieren or shadowgraph arrangements, have been reviewed by Geohegan [33]. Two-dimensional, species resolved holographic interferometry was used by Lindley et al. [66] and Gilgenbach et al. [35] to measure absolute-line-density profiles of KrF laser-generated aluminum plumes in vacuum and argon atmospheres. Direct acquisition of emission spectra led to derivation of vibrational temperatures and estimates of radical concentrations [20]. Density gradients in a laser-generated plume can be monitored by the deflection of a probe laser in the far field, as shown by Enloe et al. [25] and Chen and Yeung [19]. With sophisticated numerical modeling and detailed experimental, it will be possible to advance important applications such as the pulsed laser deposition (PLD). This technique has been drawing significant attention in the scientific community, having enabled fabrication of novel thin film materials of high quality and superior properties as compared to conventional manufacturing techniques.

IV. Conclusions

In this chapter, recent research on pulsed-laser-induced phase-change transformations at the nanosecond time scale was reviewed. The melting of semiconductor materials was probed by optical reflectance, transmittance, electrical conductance, and infrared pyrometry. The experimental results were in general agreement with the thermal model, except for the high-irradiance regime. Direct measurements of the solid–liquid interface

in melting of polysilicon films on glass substrates showed superheat by over 100°C. The rapid mass transfer in the liquid silicon phase allowed successful fabrication of well-controlled and sharply defined box-shaped ultrashallow dopant junction profiles. Annealing of gold was examined next. Utilizing heat transfer and stability analysis, the generation of surface morphology was attributed to Rayleigh–Taylor instability triggered by the reduction of density on melting. Time-of-flight measurements of the kinetic energy distribution in near-threshold sputtering of gold produced values exceeding the thermal model expectations. A computational heat transfer analysis of the heat transfer and the vapor gas dynamics adopting the transparent vapor assumption was discussed. More indepth experimental and theoretical studies are needed to resolve the fundamental mechanisms of ablation from the liquid or the solid phases.

Acknowledgment

Nomenclature

a	acceleration	$C_1 = 3.7420 \times 10^8$	
A	area	$W/\mu m^4/m^2$	
A_d	particle detector area	C_2	blackbody radiation constant,
a_1, a_2, a_3	constants in the vapor pressure–temperature relation [Eq. (55)]	$C_2 = 1.4388 \times 10^4 \ \mu m \ K$	
		C_3	material constant for the kinetic rate of solid–liquid transformation
C	dopant concentration		mation
C'	constant in phase-change kinetic relation	D	mass diffusivity
		d_j	junction depth
C_p	specific heat for constant pressure	Δd_j	junction transition depth
		d_{ab}	optical absorption depth
C_s	sonic speed	d_{ss}	substrate thickness
C_v	specific heat for constant volume	dA	area on the laser-heated spot whose thermal emission is detected by the detector
C_0	dopant concentration at the surface	D_d	droplet diameter
C_1	blackbody radiation constant,	e	specific internal energy

E	translational energy of ejected particles	R_F^0	rate of solidification at equilibrium
E_t	total energy per unit mass	t	time
E_0	energy of the laser pulse	T	temperature
$e_{\lambda b}$	blackbody emissive power	T_{int}	interface temperature
f	distribution of molecules per unit volume	T_M	equilibrium melting temperature
F	laser fluence	T_0	elevated target temperature
h	Planck's constant	$\mathbf{u}$	velocity vector of ejected particles
H	enthalpy		
I	laser intensity profile	v_e	propagation velocity of dilatational waves
i	imaginary unit		
j_{ev}	evaporation rate	V	voltage recorded on the oscilloscope
k	thermal conductivity		
k_B	Boltzmann constant	$\mathbf{V}$	velocity vector
k_{ext}	extinction coefficient	V_{int}	interfacial velocity
l	length of silicon strip	w	width of silicon strip
L_m	latent heat of fusion	x	coordinate in the normal to the sample surface direction
L_v	latent heat of vaporization		
$\dot{m}_{ev}$	evaporation mass flow rate	x, y, z	coordinates in a Cartesian system
m	mass per atom		
M_r	recoil momentum	X_{int}	transient location of the interface from the surface of the solid layer at $t = 0$
n	real part of refractive index		
N	laser pulse number		
N_d	number density signal at the detector		
n_i	number of ions per unit volume	SUBSCRIPTS	
n_l	number of liquid atoms per unit volume		
		ev	evaporation
		exc	excimer laser
n_n	number of neutrals per unit volume	int	solid–liquid interface
		l	liquid
n_s	number density of ejected particles at the surface	s	solid
		ss	substrate
n_v	number of vapor atoms per unit volume	v	vapor phase
		∞	ambient conditions
$\hat{n}$	complex refractive index		
P	pressure		
P_{recoil}	recoil pressure [Eq. (63)]	SUPERSCRIPTS	
Q	activation energy		
Q_{ab}	power absorbed	$'$	directional
r	coordinate in the radial direction	$*$	normalized variables
r_{las}	laser beam radius		
R	reflectivity	HATS	
R_s	specular reflectivity		
R_d	diffuse reflectivity	$\sim$	quantity accounting for stream velocity formation at the edge of the Knudsen layer
R_M	rate of melting		
R_M^0	rate of melting at equilibrium		
R_F	rate of solidification	$-$	mean quantity

GREEK		θ_i	incident angle
		θ_s	sticking coefficient
α	absorptivity	λ	laser light wavelength
α_{th}	thermal expansion coefficient	Λ	Constant in the density–
γ	ratio of the specific heats ($\gamma =$		temperature relation
	C_p/C_v)		[Eq. (56)]
Γ	parameter in Eq. (47) [$\Gamma^2 =$	λ_D	most dangerous perturbation
	$m/(2k_BT)$]		wavelength
δ_m	melting depth	ν	light frequency
δ_T	thermal penetration depth in the	ρ	density
	target solid	σ	surface tension
ΔT	interfacial undercooling ($\Delta T =$	σ_{el}	electric conductivity
	$T_m - T_{int}$)	τ	transmissivity of optics
ΔT_p	average rise in temperature over	τ_p	laser pulse duration
	the thermal penetration depth	τ_m	melting duration
ε	emissivity	τ_{mech}	time scale for mechanical
η	absorption coefficient		expansion of target solid
θ	polar angle	ϕ	azimuthal angle
θ_d	detector angle	Ω	electric resistance

References

1. Aden, M., Beyer, E., and Herziger, G. (1990). Laser-induced vaporization of metal as a Riemann problem. *J. Phys. D* **23**, 655–661.

2. Aden, M., Beyer, E., Herziger, G., and Kunze, H. (1992). Laser-induced vaporization of a metal surface. *J. Phys. D* **25**, 57–65.

3. Afanas'ev, Y. V., and Krokhin, O. N. (1967). Vaporization of matter exposed to laser emission. *Sov. Phys.—JETP (Engl. Transl.)* **25**(4), 639–645.

4. Anisimov, S. I. (1968). Vaporization of metal absorbing laser radiation. *Sov. Phys.--JETP (Engl. Transl.)* **27**(1), 182–183.

5. Atthey, D. R. (1974). A finite difference scheme for melting problems. *J. Inst. Math. Appl.* **13**, 353–365.

6. Baeri, P., Campisano, S. U., Rimini, E., and Zhang, J. P. (1984). Time-resolved temperature measurement of pulsed laser irradiated germanuim by thin film thermocouple. *Appl. Phys. Lett.* **45**(4), 398–400.

7. Batanov, V. A., Bunkin, F. V., Prokhorov, A. M., and Fedorov, V. B. (1972). Evaporation of metallic targets caused by intense optical radiation. *Zh. Eksp. Teor. Fiz.* **63**, 586–608.

8. Bennett, F. D. (1971). Vaporization-wave transitions. In *Physics of High Energy Density* (P. Caldirola and H. Knoepfel, eds.), pp. 217–229, Academic Press, New York.

9. Bennett, T. D., Grigoropoulos, C. P., and Krajnovich, D. J. (1995). Near-threshold laser sputtering of gold. *J. Appl. Phys.* **77**(2), 849–864.

10. Bennett, T. D., Krajnovich, D. J., and Grigoropoulos, C. P. (1996). Separating thermal, electronic, and topography effects in pulsed laser melting and sputtering of gold, *Phys. Rev. Lett.* (in press).

11. Bird, G. A. (1976). *Molecular Gas Dynamics*. Oxford Univ. Press (Clarendon), London.

12. Boneberg, J., Yavas, O., Mierswa, B., and Leiderer, P. (1992). Optical reflectivity of Si above the melting point. *Phys. Status Solidi B* **174**, 295–300.

13. Bourdon, E. B. D., Das, P., Harrison, I., Polanyi, J. C., Segner, J., Stanners, C. D., Williams, R. J., and Young, P. A. (1986). Photodissociation, photoreaction and photodesorption of absorbed species. *Faraday Discuss. Chem. Soc.* **82**, 343–358.

14. Bruines, J. J. P., van Hal, R. P. M., Boots, H. M. J., Sinke, W., and Saris, F. W. (1986). Direct observation of resolidification from the surface upon pulsed-laser melting of amorphous silicon. *Appl. Phys. Lett.* **48**(19), 1252–1254.

15. Carey, V. P. (1992). *Liquid-Vapor Phase-Change Phenomena*. Hemisphere Publishing, Bristol, PA.

16. Chan, C. L., and Mazumder, J. (1987). One-dimensional steady-state model for damage by vaporization and liquid expulsion due to laser-material ablation. *J. Appl. Phys.* **62**(11), 4579–4586.

17. Chandrasekhar, S. (1981). *Hydrodynamic and Hydromagnetic Stability*. Dover Publ., New York.

18. Chen, F. F. (1984). *Introduction to Plasma Physics and Controlled Fusion*, 2nd ed., Vol. I. Plenum, New York.

19. Chen, G., and Yeung, E. S. (1988). A spatial and temporal probe for laser-generated plumes based on density gradients. *Anal. Chem.* **60**, 864–868.

20. Chen, X., Mazumder, J., and Purohit, A. (1991). Optical emission diagnostics of laser-induced plasma for diamond-like film deposition. *Appl. Phys. A* **52**, 328–334.

20a. Chrisey, D. B., and Hubler, G. K. (1994). *Pulsed Laser Deposition of Thin Films*. John Wiley, New York.

21. Colella, P. (1985). A direct Eulerian MUSCL scheme for gas dynamics. *SIAM J. Sci. Stat. Comput.* **6**(1), 104–117.

22. Dlott, D. D. (1990). Ultrafast vibrational energy transfer in the real world: Laser ablation, energetic solids, and hemeproteins. *J. Opt. Soc. Am. B* **7**(8), 1638–1652.

23. Duzy, C., Knight, C. J., Woodroffe, I. A., and Young, L. A. (1981). *Analysis of Ultraviolet and Visible Laser Effects*, AVCO Final Tech. Rep., Everett Res. Lab., Everett, MA.

24. Eidel'man, E. D. (1994). Instability due to thermocapillary and thermoelectric effects in liquid semiconductors. *Semiconductors* **28**(9), 858–862.

25. Enloe, C. L. Gilgenbach, R. M., and Meachum, J. S. (1987). Fast, sensitive laser deflection system suitable for transient plasma analysis. *Rev. Sci. Instrum.* **58**(9), 1597–1600.

26. Eryu, O., Murakami, K., Masuda, K., Kasuya, A., and Nishina, Y. (1989). Dynamics of laser-ablated particles from high Tc superconductor $YBa_2Cu_3O_y$. *Appl. Phys. Lett.* **54**(26), 2716–2718.

27. Fann, W. S., Storz, R., Tom, H. W. K., and Bokor, J. (1992). Electron thermalization in gold. *Phys. Rev. B* **46**(20), 13592–13595.

28. Fauchet, P. M., and Siegman, A. E. (1983). Observations of higher-order laser-induced surface ripples on $\langle 111 \rangle$ germanium. *Appl. Phys. A* **32**, 135–140.

29. Finke, B. R., and Simon, G. (1990). On the gas kinetics of laser-induced evaporation of metals. *J. Phys. D* **23**, 67–74.

30. Finke, B. R., Finke, M., Kapadia, P. D., Dowden, J. M., and Simon, G. (1990). Numerical investigation of the Knudsen layer appearing in the laser-induced evaporation of metals. *Proc. SPIE* **1279**, 127–134.

31. Galvin, G. J., Thompson, M. O., Mayer, J. W., Hammond, R. B., Paulter, N., and Peercy, P. S. (1982). Measurement of the velocity of the crystal-liquid interface in pulsed laser annealing of Si. *Phys. Rev. Lett.* **48**(1), 33–36.

32. Geohegan, D. B. (1992). Fast intensified-CCD photography of $YBa_2Cu_3O_{7-x}$ laser ablation in vacuum and ambient oxygen. *Appl. Phys. Lett.* **60**(22), 2732–2734.

33. Geohegan, D. B. (1994). Diagnostics and characteristics of pulsed laser deposition laser plasmas. In *Pulsed Laser Deposition of Thin Films* (D. B. Chrisey and G. K. Hubler, eds.), pp. 115–165, Wiley, New York.

34. Gibert, T., Dubreuil, B., Barthe, M. F., and Debrun, J. L. (1993). Investigation of laser sputtering of iron at low fluence using resonance ionization mass spectrometry. *J. Appl. Phys.* **74**(5), 3506–3513.

35. Gilgenbach, R. M., Ching, C. H., Lash, J. S., and Lindley, R. A. (1994). Laser diagnostic experiments of KrF laser ablation plasma-plume dynamics relevant to manufacturing applications. *Phys. Plasmas* **1**(5), 1619–1625.

36. Glazov, V. N., Chizhevskaya, S. N., and Glagoleva, N. N. (1969). *Liquid Semiconductors.* Plunum, New York.

37. Heitz, J., Arenholz, E., Bauerle, D., Sauerbrey, R., and Phillips, H. M. (1994). Femtosecond excimer-laser-induced structure formation on polymers. *Appl. Phys. A* **59**, 289–293.

38. Ho, J.-R., Grigoropoulos, C. P., and Humphrey, J. A. C. (1996). Gas dynamics and radiation heat transfer in the vapor plume produced by pulsed laser irradiation of aluminum. *J. Appl. Phys.* (in press).

39. Ho, J.-R., Grigoropoulos, C. P., and Humphrey, J. A. C. (1995). Computational model for the heat transfer and gas dynamics in the pulsed laser evaporation of metals. *J. Appl. Phys.* **78**(6), 4696–4709.

40. Hoheisel, W., Vollmer, M., and Träger, F. (1993). Desorption of metal atoms with laser light: Mechanistic studies. *Phys. Rev. B* **48**(23), 17463–17476.

41. Iida, T., and Guthrie, R. I. L. (1993). *The Physical Properties of Liquid Metals.* Oxford Univ. Press (Claredon), Oxford.

42. Im, J. S., Kim, H. J., and Thompson, M. O. (1993). Phase transformation mechanisms involved in excimer laser crystallization of amorphous silicon films. *Appl. Phys. Lett.* **63**(14), 1969–1971.

43. Jackson, K. A. (1975). Theory of melt growth. In *Crystal Growth and Characterization* (R. Ueda and J. B. Mullin, eds.), pp. 21–32. North-Holland Publ., Amsterdam.

44. Jackson, K. A., and Chalmers, B. (1956). Kinetics of solidification, *Can. J. Phys.* **34**, 473–490.

45. Jellison, G. E. Jr., and Lowndes, D. H. (1985). Time-resolved ellipsometry and reflectivity measurements of the optical properties of sillicon during pulsed excimer laser irradiation. *Proc. Mater. Res. Soc.* **35**, 113–118.

46. Jellison, G. E. Jr., Lowndes, D. H., Mashburn, D. N., and Wood, R. F. (1986). Time-resolved reflectivity measurements on sillicon and germanium using a pulsed excimer KrF laser heating beam. *Phys. Rev. B* **34**(4), 2407–2415.

47. Kelly, R. (1990). On the dual role of the Knudsen layer and unsteady, adiabatic expansion in pulse sputtering phenomena. *J. Chem. Phys.* **92**(8), 5047–5056.

48. Kelly, R. (1992). Gas dynamics of the pulsed emission of a perfect gas with applications to laser sputtering and to nozzle expansion. *Phys. Rev. A* **46**(2), 860–874.

49. Kelly R., and Dreyfus, R. W. (1988). Reconsidering the mechanisms of laser sputtering with Knudsen-layer formation taken into account. *Nucl. Instrum. Methods Phys. Res. Sect. B* **32**, 341–348.

50. Kelly, R., and Dreyfus, R. W. (1988). On the effect of Knudsen-layer formation on studies of vaporization, sputtering and desorption. *Surf. Sci.* **198**, 263–276.

51. Kelly, R., and Rothenberg, J. E. (1985). Laser sputtering: Part III. The mechanism of the sputtering of metals at low energy densities. *Nucl. Instrum. Methods Phys. Res. Sect. B* **7/8**, 755–763.

52. Kelly, R., Cuomo, J. J., Leary, P. A., Rothenberg, J. E., Braren, B. E., and Aliotta, C. F. (1985). Laser Sputtering: Part I. On the existence of rapid laser sputtering at 193 nm. *Nucl. Instrum. Methods. Phys. Res. Sect. B* **9**, 329–340.

53. Kim, J., and Helvajian, H. (1994). Laser-induced ion species ejection from thin silver films: Influence of plasmon excitation on the desorbed species KE distributions. In *Laser Ablation: Mechanisms and Applications II* (J. C. Miller and D. B. Geohegan, eds.), pp. 38–43, American Institute of Physics Press, New York.

54. Kim, W. S., Hector, L. G. Jr., and Ozisik, M. N. (1990). Hyperbolic heat conduction due to axisymmetric continuous or pulsed surface heat sources. *J. Appl. Phys.* **68**(11), 5478–5485.

55. Kittl, J. A., Reitano, R., Aziz, M. J., Brunco, D. P., and Thompson, M. O. (1993). Time-resolved temperature measurements during rapid solidification of Si-As alloys induced by pulsed-laser melting. *J. Appl. Phys.* **73**(8), 3725–3733.

56. Kluge, M. D., and Ray, J. R. (1989). Velocity versus temperature relation for solidification and melting of silicon. *Phys. Rev. B* **39**(3), 1738–1746.

57. Knight, C. J. (1976). Evaporation from a cylindrical surface into vacuum. *J. Fluid Mech.* **75**(3), 469–486.

58. Kondera, H. (1963). Diffusion coefficients of impurities in silicon melt. *Jp. J. Appl. Phys.* **2**, 212–219.

59. Koren, G., Gupta, A., Baseman, R. J., Lutwyche, M. I., and Laibowitz, R. B. (1989). Laser wavelength dependent properties of $YBa_2Cu_3O_{7-\delta}$ thin films deposited by laser ablation. *Appl. Phys. Lett.* **55**(23), 2450–2452.

60. Krajnovich, D. J. (1995). Laser sputtering of highly oriented pyrolytic graphite at 248 nm. *J. Chem. Phys.* **102**, 726–743.

61. Krajnovich, D. J., and Vazquez, J. E. (1993). Formation of 'intrinsic' surface defects during 248 nm photoablation of polyimide. *J. Appl. Phys.* **73**(6), 3001–3008.

62. Krebs, H.-U., and Bremert, O. (1993). Pulsed laser deposition of thin metallic alloys. *Appl. Phys. Lett.* **62**(19), 2341–2343.

63. Landi, E., Carey, P. G., and Sigmon, T. W. (1988). Numerical simulation of the gas immersion laser doping (GILD) process in silicon. *IEEE Trans. Comput.-Aided Des.* **CAD-7**(2), 205–213.

64. Larson, B. C., White, C. W., Noggle, T. S., Barhorst, J. F., and Mills, D. M. (1983). Time-resolved study of silicon during pulsed-laser annealing. *Proc. Mater. Res. Soc.* **13**, 43–50.

65. Lee, I., Callcott, T. A., and Arakawa, E. T. (1993). Desorption studies of metal atoms using laser-induced surface-plasmon excitation. *Phys. Rev. B* **47**, 6661–6666.

66. Lindley, R. A., Gilgenbach, R. M., and Ching, C. H. (1993). Resonant holographic interferometry of laser-ablation plumes. *Appl. Phys. Lett.* **63**(7), 888–890.

67. Lowndes, D. H., Penycook, S. J., Jellison, G. E. Jr., Withrow, S. P., and Mashburn, D. N. (1987). Solidification of highly undercooled liquid silicon produced by pulsed laser melting of ion-implanted amorphous silicon: Time-resolved and microstructural studies. *J. Mater. Res.* **2**(5), 648–680.

68. Matsumoto, S., Yoshioka, S., Wada, J., Inui, S., and Uwasawa, K. (1990). Boron doping of silicon by ArF excimer laser irradiation in B_2H_6. *J. Appl. Phys.* **67**(12), 7204–7210.

69. Miller, J. C., ed. (1994). *Laser Ablation*. Springer-Verlag, Heidelberg.

70. Misra, D. S., and Palmer, S. B. (1991). Laser ablated thin films of $Y_1Ba_2Cu_3O_{7-\delta}$: The nature and origin of the particulates. *Physica C* **176**, 43–48.

71. O'Brien, T. P., Lawler, J. F., Lunney, J. G., and Blau, W. J. (1992). The effect of laser fluence on the ablation and deposition of $YBa_2Cu_3O_7$. *Mater. Sci. Eng.* **B13**, 9–13.

72. Okada, T., Shibamaru, N., Nakayama, Y., and Maeda, M. (1992). Investigations of behavior of particles generated from laser-ablated $YBa_2Cu_3O_{7-x}$ target using laser-induced fluorescence. *Appl. Phys. Lett.* **60**(8), 941–943.

73. Okada, T., Nakayama, Y., Kumuduni, W. K. A., and Maeda, M. (1992). Observation of scattering of particles produced by laser ablation on a substrate by laser induced fluorescence. *Appl. Phys. Lett.* **61**(19), 2368–2370.

74. Olstad, R. A., and Olander, D. R. (1975). Evaporation of solids by laser pulses. I. Iron. *J. Appl. Phys.* **46**(4), 1499–1508.

75. Ozisik, M. N., and Tzou, D. Y. (1994). On the wave theory in heat conduction. *J. Heat Transfer* **116**, 526–535.

76. Pamler, W., and Marinero, E. E. (1987). Transient conductivity studies in tellurium thin films. *J. Appl. Phys.* **61**(6), 2294–2300.

77. Phipps, C. R. Jr., and Dreyfus, R. W. (1993). The high laser irradiance regime. In *Laser Ionization Mass Analysis* (A. Vertes, R. Gijbels, and F. Adams, eds.), pp. 369–431, Wiley, New York.

78. Phipps, C. R. Jr., Turner, T. P., Harrison, R. F., York, G. W., Osborne, W. Z., Anderson, G. K., Corlis, X. F., Haynes, L. C., Steele, H. S., Spicochi, K. C., and King, T. R. (1988). Impulse coupling to targets in vacuum by KrF, HF, and CO_2 single-pulse lasers. *J. Appl. Phys.* **64**(3), 1083–1096.

79. Pospieszczyk, A., Harith, M. A., and Stritzker, B. (1983). Pulsed laser annealing of GaAs and Si: Combined reflectivity and time-of-flight measurements. *J. Appl. Phys.* **54**(6), 3176–3182.

80. Qiu, T. Q., and Tien, C.-L. (1992). Short-pulse laser heating on metals. *Int. J. Heat. Mass Transfer* **35**, 719–726.

81. Ritchie, R. H. (1973). Surface plasmons in solids. *Surf. Sci.* **34**, 1–19.

82. Ritchie, R. H., Manson, J. R., and Echenique, P. M. (1994). Surface-plasmon-ion interaction in laser ablation of ions from a surface. *Phys. Rev. B* **49**, 2963–2966.

83. Rosen, D. I., Mitteldorf, J., Kothandaramaran, G., Pirri, A. N., and Pugh, E. R. (1982). Coupling of pulsed 0.35-μm laser radiation to aluminum alloys. *J. Appl. Phys.* **53**(4), 3190–3200.

84. Rykalin, N., Uglov, A., Zuev, I., and Kokora, A. (1988). *Laser and Electron Beam Materials Processing Handbook.* MIR Publishers, Moscow.

85. Sameshima, T., and Usui, S. (1993). Pulsed laser-induced melting followed by quenching of silicon films. *J. Appl. Phys.* **74**(11), 6592–6598.

86. Sasik, R., and Cerny, R. (1991). Numerical solution of the non-isothermal moving boundary problem in heat conduction. *Comput. Phys. Commun.* **64**, 241–251.

87. Scarfone, C., Norton, M. G., Carter, C. B., Li, J., and Mayer, J. W. (1991). Characterization of $BaTiO_3$ thin films Deposited by pulsed laser ablation. *Proc. Mater. Res. Soc.* (H. A. Atwater *et al.* ed.) 183–188.

88. Scheibe, H.-J., Gorbunov, A. A., Baranova, G. K., Klassen, N. V., Konov, V. I., Kulakov, M. P., Pompe, W., Prokhorov, A. M., and Weiss, H.-J. (1991). Thin film deposition by excimer laser evaporation. *Thin Solid Films* **189**, 283–291.

89. Shamsundar, N., and Sparrow, E. M. (1975). Analysis of multidimensional conduction phase change via the enthalpy model. *J. Heat Transfer* **97**, 333–340.

90. Shea, M. J., and Compton, R. N. (1993). Surface-plasmon ejection of Ag^+ ions from laser irradiation of a roughened silver surface. *Phys. Rev. B* **47**, 9967–9970.

91. Shvarev, K. M., Baum, B. A., and Gel'd, P. V. (1975). Optical properties of liquid silicon. *Sov. Phys.—Solid State (Engl. Transl.)* **16**(11), 2111–2112.

92. Sibold, D., and Urbassek, H. M. (1991). Kinetic study of pulsed desorption flaws into vacuum. *Phys. Rev. A* **43**, 6722–6734.

93. Singh, R. K., and Narayan, J. (1990). Pulsed-laser evaporation technique for deposition of thin films: Physics and theoretical model. *Phys. Rev. B* **41**(13), 8843–8859.

94. Sipe, J. E., Young, J. F., Preston, J. S., and van Driel, H. M. (1983). Laser-induced periodic surface structure. *Phys. Rev. B* **27**(2), 1141–1154.

95. Slack, G. A. (1964). Thermal conductivity of pure and impure silicon, silicon carbide, and diamond. *J. Appl. Phys.* **35**(12), 3460–3466.

96. Stritzker, B., Pospieszcyk, A., and Tagle, J. A. (1981). Measurement of lattice temperature of silicon during laser annealing. *Phys. Rev. Lett.* **47**(5), 356–358.

97. Tabor, D. (1991). *Gases, Liquids and Solids*, 3rd ed. Cambridge Univ. Press, Cambridge.

98. Tai, Y. C., Mastrangelo, C. H., and Muller, R. S. (1988). Thermal conductivity of heavily doped low-pressure chemical vapor deposited polycrystalline silicon films. *J. Appl. Phys.* **63**(5), 1442–1447.

99. Tokarev, V. N., and Konov, V. I. (1994). Suppression of thermocapillary waves in laser melting of metals and semiconductors. *J. Appl. Phys.* **76**(2), 800–805.

100. Tsao, J. Y., Picraux, S. T., Peercy, P. S., and Thompson, M. O. (1986). Direct measurements of liquid/solid interface kinetics during pulsed-laser-induced melting of aluminum. *Appl. Phys. Lett.* **48**(4), 278–280.

101. Van de Riet, E., Nillesen, J. C. M., and Dieleman, J. (1993). Reduction of droplet emission and target roughening in laser ablation and deposition of metals. *J. Appl. Phys.* **74**(3), 2008–2012.

102. Vertes, A., Juhasz, P., De Wolf, M., and Gijbels, R. (1989). Hydrodynamic modelling of laser plasma ionization processes. *Int. J. Mass Spectrom. Ion Processes* **94**, 63–85.

103. Vertes, A., Gijbels, R., and Adams, F., eds. (1993). *Laser Ionization Mass Analysis.* Wiley, New York.

104. von Allmen, M. (1987). *Laser-Beam Interactions with Materials.* Springer-Verlag, Heidelberg.

105. Weiner, K. H., Carey, P. G., McGarthy, A. M., and Sigmon, T. W. (1993). An excimer-laser-based nanosecond thermal diffusion technique for ultra-shallow pn junction fabrication. *Microelectron. Eng.* **20**, 107–130.

106. Wilson, R. G., Stevie, F. A., and Magee, C. W. (1989). *Secondary Ion Mass Spectrometry: A Practical Handbook for Depth Profiling and Bulk Impurity Analysis*, pp. 3.1.1–3.2.4, Wiley, New York.

107. Wolf, S., and Tauber, R. N. (1986). *Silicon Processing for the VLSI Era*, Vol. 1, p. 251, Lattice Press, Sunset Beach, CA.

108. Wood, R. F., and Geist, G. A. (1986). Theoretical analysis of explosively propagating molten layers in pulsed laser-irradiated a-Si. *Phys. Rev. Lett.* **57**(7), 873–876.

109. Wood, R. F., and Geist, G. A. (1986). Modeling of nonequilibrium melting and solidification in laser-irradiated materials. *Phys. Rev. B* **34**(4), 2606–2620.

110. Wood, R. F., and Giles, G. E. (1981). Macroscopic theory of pulsed-laser annealing. I. Thermal transport and melting. *Phys. Rev. B* **23**(6), 2923–2942.

111. Wood, R. F., and Jellison, G. E. Jr. (1984). melting model of the pulsed laser process. *Semicond. Semimetals* **23**, 165–250.

112. Young, J. F., Sipe, J. E., Preston, J. S., and van Driel, H. M. (1982). Laser-induced periodic surface damage and radiation remnants. *Appl. Phys. Lett.*, **41**(3), 261–264.

113. Xu, X., Grigoropoulos, C. P., and Russo, R. E. (1994). Measurement of solid/liquid interface temperature during pulsed excimer laser melting of polysilicon films. *Appl. Phys. Lett.* **65**(14), 1745–1747.

114. Xu, X., Grigoropoulos, C. P., and Russo, R. E. (1995). Heat transfer in excimer laser melting of thin silicon films. *J. Heat Transfer* **117**, 708–715.

115. Xu, X., Grigoropoulos, C. P., and Russo, R. E. (1995). Nanosecond time resolution thermal emission measurement during pulsed excimer laser interaction with materials. *Appl. Phys. A* (in press).
116. Zel'dovich, Ya. B., and Raizer, Yu. P. (1967). *Physics of Shock Waves and High Temperature Hydrodynamic Phenomena*, Vols. 1–2. Academic Press, New York.
117. Zhang, X., Ho, J.-R., and Grigoropoulos, C. P. (1996). Ultra-shallow p^+-junction formation in silicon by excimer laser doping with a solid dopant film. *Int. J. Heat Mass Transfer*, to appear.
118. Zheng, J. P., Huang, Z. Q., Shaw, D. T., and Kwok, H. S. (1989). Generation of high-energy atomic beams in laser-superconducting target interactions. *Appl. Phys. Lett.* **54**(3), 280–282.
119. Zheng, J. P., Ying, Q. Y., Wianachchi, S., Haung, Z. Q., Shaw, D. T., and Kwok, H. S. (1989). Role of the oxygen atomic beam in low-temperature growth of superconducting films by laser deposition. *Appl. Phys. Lett.* **54**(10), 954–956.